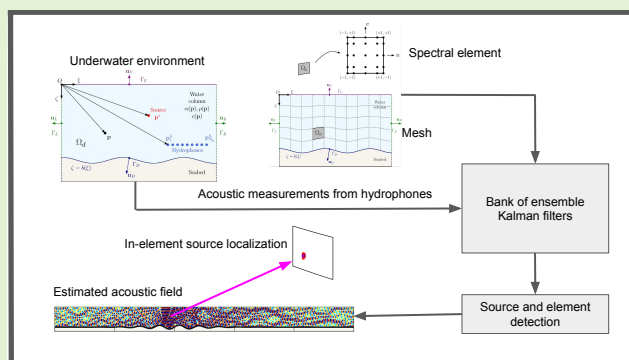# Underwater Source Localization via Spectral Element Acoustic Field Estimation

G.A. Manduzio, N. Forti, R. Sabatini, G. Battistelli, and L. Chisci

Abstract— **Underwater source localization from a passive array of acoustic sensors is a challenging problem, especially in complex environments characterized by multipath and reverberation effects, irregular seabed geometry, and low signal-to-noise ratio. This paper proposes a recursive Bayesian approach that propagates a spectral-element approximation of the wave equation to model the discretized space-time dynamics of the acoustic field conditioned on the position of the source, and sequentially estimates the field and the position of the radiating source from the acoustic measurements. We pursue a multiple-model approach where each model assumes either the source absence or its presence within a specific spectral element. To handle the high dimension of the large-scale field estimation problem and reduce the computational complexity, the multiple-model filter is implemented by using ensemble Kalman filters. Finally, the effectiveness of the proposed multiple-model spectral-element ensemble Kalman filter is demonstrated through simulation experiments in underwater acoustic environments with regular and irregular seabed geometry and via comparison with the standard matched-field processing method.**

Index Terms— **Acoustic Field Estimation, Ensemble Kalman Filter, Multiple-Model Filtering, Spectral Element Method, Underwater Source Localization**

I. INTRODUCTION

UNDERWATER source localization (USL) using a passive array of acoustic sensors aims at detecting a radiating source and estimating its position in space by analyzing the acoustic field measured by an array of hydrophones. Due to the special characteristics and complexity of the underwater environment, USL using a passive array of acoustic sensors is a challenging task, attracting great interest within both the control and signal processing communities, especially in low *signal-to-noise ratio* (SNR) scenarios where the source can be difficult to detect [1]. When the source is in the *far-field* of the sensor array, i.e. far enough for the plane-wave approximation to be valid, conventional passive sonar systems based on array signal processing can only estimate the *direction of arrival* (DOA) of an acoustic signal impinging on the array via plane-wave beamforming [1], [2]. DOA is determined by

using the time differences of the sound arrival among the spatially-separated hydrophones of the array. This is the main difference from active sonar systems where the absolute time of signal transmission from a projector is known, also allowing estimation of the range from the sonar system to the source of interest. In addition to conventional beamforming, other DOA estimation methods have been developed and applied to USL [3], including subspace-based approaches such as *multiple signal classification* (MUSIC), *estimation of signal parameters via rotational invariance technique* (ESPRIT), and their modifications [4].

In low SNR environments, the major practical challenge is to extract the DOA information from acoustic signals that are distorted by different types of noise (e.g., ambient, measurement, and thermal noise). In fact, classical methods based on DOA estimation can only exploit thresholded measurements. Then, for low SNRs, the received signals are more likely to be undetected using conventional DOA methods since the information contained in the measurements may be irreversibly discarded after the thresholding process [5]–[7]. Moreover, in realistic underwater environments, DOA estimation methods can be highly affected by multipath and reverberation effects, inhomogeneous domains, and irregular seabed geometries, resulting in inaccurate localization. In such scenarios, acoustic propagation and its effects can be exploited to enable passive localization. To this end, the major developments in underwater passive localization since the early 1980s have focused on the inclusion of acoustic

G.A. Manduzio is with the Dipartimento di Ingegneria dell'Informazione, Università di Pisa, 56122 Pisa, Italy (e-mail: grazianoalfredo.manduzio@phd.unipi.it).

N. Forti was with the NATO Science and Technology Organization Centre for Maritime Research and Experimentation, 19126 La Spezia, Italy. He is currently with the Dipartimento di Ingegneria dell'Informazione, Università degli Studi di Firenze, 50139 Firenze, Italy (e-mail: nicola.forti@unifi.it).

G. Battistelli, and L. Chisci are with the Dipartimento di Ingegneria dell'Informazione, Università degli Studi di Firenze, 50139 Firenze, Italy (e-mail: {giorgio.battistelli,luigi.chisci}@unifi.it).

R. Sabatini is with the Department of Physical Sciences and the Center for Space and Atmospheric Research at Embry-Riddle Aeronautical University, Daytona Beach, Florida, 32114 USA (e-mail: sabatinr@erau.edu).
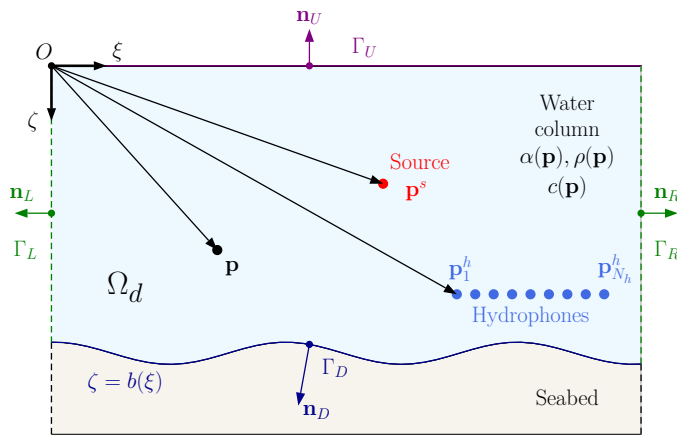
Fig. 1: Sketch of the source localization problem in an underwater acoustic environment.

propagation modeling into signal processing algorithms [8]. When the acoustic propagation model is accounted for in the passive sonar array signal processing, we refer to the procedure as *matched-field processing* (MFP) [9]–[12]. MFP is a well-established generalization of plane-wave beamforming for USL where the *steering* or *replica* vector is derived from a solution of the wave equation in the frequency domain (i.e., the Helmholtz equation) for a point source, especially common for shallow water applications where multipath propagation can yield useful information to infer the source range and depth. MFP is based on matching (correlating) the acoustic pressure field measured at the hydrophone array with modeled *replica* fields computed for a given acoustic waveguide environment via a numerical propagation model over a set of test source positions, typically distributed over a uniform search grid covering the given range-depth domain. The maximum in the cross-correlation or ambiguity surface gives an estimate of the position of the underwater source, usually taken to be the grid point associated to the highest match. Source localization using common MFP is effective when the source is already detected and stationary, its frequency is known, and there is full knowledge of the propagation model. However, it can be highly degraded or precluded in the case of inaccurate correspondence (mismatch) between the propagation model and the real oceanic waveguide, i.e., for noisy or uncertain source and environmental parameters [13]–[15]. To improve USL performance, MFP approaches combining information from multiple arrays have recently been studied for shallow-water scenarios [16], [17]. It is demonstrated that spatially coherent processing of multiple arrays can yield significant improvement in localization performance over incoherent processing. However, it can also be more susceptible to model mismatch than incoherent processing.

The main challenge of USL is to devise estimators which are less sensitive to the noise level and environmental mismatch. Conventional MFP methods rely on numerically efficient propagation models such as normal modes that are not capable of treating inhomogeneous environments with complex geometry characterizing scattering and reverberation problems. More general numerical methods based on direct discretization of the governing full wave equation include the finite difference and *finite element method* (FEM). In particular, FEM is extremely versatile in terms of geometries and environment properties that can be treated, and boundary conditions as well as point sources can be directly incorporated in its formulation. However, with increasing frequencies, the FEM mesh requires a growing number of finite elements, thus resulting in increased computational time. The *spectral element method* (SEM) [18]–[20] is a particular kind of FEM that uses high-degree piecewise polynomials as basis functions within quadrangular (in 2-D) or hexahedral (in 3-D) elements. The SEM provides high accuracy with fewer degrees of freedom in comparison with the standard FEM. Moreover, it employs non-uniformly distributed nodes, the so-called Gauss-Lobatto-Legendre points, and, when used in conjunction with the Gauss-Lobatto-Legendre quadrature rule, results in a diagonal mass matrix, allowing for reduced complexity, computational time and memory.

This work exploits recent advancements in numerical simulation of *partial differential equation* (PDE) systems [18]–[22] to approximate the wave equation into a finite-dimensional space-time model of the underwater acoustic field. Additionally, this paper builds on large-scale field estimation of discretized PDE systems [23], [24], and previous work on source identifiability and estimation in such systems [25], [26]. Further related work focused on USL for shallow-water environments and high-frequency signals using a multi-ray propagation model [27], decentralized detection in underwater sensor networks [28], decentralized USL via generalized likelihood ratio test [29], a self-supervised learning architecture that exploits joint time-frequency processing for USL [30], and acoustic source localization and tracking using a cluster of mobile agents [31].

This paper presents a novel *multiple-model spectral-element ensemble Kalman filter* (MM-SE-EnKF) algorithm for underwater source detection and localization. The proposed method incorporates a SEM-based model of underwater acoustic propagation in the time domain to sequentially estimate the acoustic field directly from acoustic pressure measurements. This allows USL in complex environments characterized by inhomogeneous properties and/or irregular seabed geometries. The *ensemble Kalman filter* (EnKF) [32] is adopted for computationally efficient acoustic field estimation. Source localization is performed by using a multiple-model approach that runs in parallel a bank of field estimators, each conditioned to the source being placed in a given element of the discretized computational domain, plus a null hypothesis accounting for the possible absence of the source. This paper improves previous work on USL using FEM-based acoustic field estimation [33] by developing a more computationally efficient SEM-based formulation of the acoustic propagation model, a faster algorithm for multiple-model estimation of the element containing the source position, and by including results in terms of USL in the case of both regular and irregular seabed geometry. Additionally, the former scenario includes a comparison of results against standard MFP. Summing up, the main contributions are as follows: (i) we provide a Bayesian formulation for the problem of joint pressure field estimation and source detection/localization directly exploiting the acoustic measurements and show how to directly integrate the SEM within the Bayesian formulation;

(ii) we develop a novel multiple-model filtering algorithm based on a bank of SE EnKFs for joint pressure field estimation and source detection/localization capable of dealing with arbitrary geometries as well as inhomogeneous properties; (iii) to improve the computational efficiency, we develop a fast algorithm in which, at each time, only the SE EnKF corresponding to the most likely mode is activated.

The rest of the paper is organized as follows. Section II describes the formulation of the considered USL problem. Section III presents a SEM-based approximation and time integration of the generalized wave equation modeling underwater acoustic propagation. In Section IV, a novel MM-SE-EnKF algorithm is proposed to address USL. Section V shows simulation results, while Section VI concludes this paper.

A. Notation

Vectors and matrices are denoted by lower-case and respectively upper-case letters in bold, while scalars are denoted by normal lower-case letters. For the reader convenience, notation and symbols used throughout the paper are listed in Table I.

II. PROBLEM FORMULATION

Consider the two-dimensional infinite oceanic waveguide Ω depicted in Fig. 1, bounded from above by a flat free surface Γ_U and from below by a possibly irregular seabed Γ_D. Define a Cartesian coordinate system $O\xi\zeta$, with origin O on Γ_U and vertical axis ζ oriented toward the seafloor, and denote by $\boldsymbol{p} \in \Omega$ the position vector and by $t \in \mathbb{R}^+$ the time variable. Let $\zeta = b(\xi)$ be the function describing the variable bathymetry, and let $\alpha(\boldsymbol{p})$, $c(\boldsymbol{p})$ and $\rho(\boldsymbol{p})$ be the assumed-known space-dependent damping coefficient, ambient speed of sound and water density, respectively. Suppose that a perturbation of pressure $x(\boldsymbol{p}, t; \boldsymbol{p}^s(t))$ is generated in the water column by a point source f located at $\boldsymbol{p}^s(t)$. The proposed algorithm aims at detecting the presence of the sound emitter and estimating its position $\boldsymbol{p}^s(t)$ and the induced acoustic field $x(\boldsymbol{p}, t; \boldsymbol{p}^s(t))$, given discrete time pressure signals $y_i(t)$, recorded by N_h sensors (hydrophones) at known locations $\boldsymbol{p}_i^h$, $i = 1, \ldots, N_h$. To this end, the propagation of the acoustic perturbation $x(\boldsymbol{p}, t; \boldsymbol{p}^s(t))$ is assumed governed by the generalized wave equation [1]

$$\frac{1}{\rho c^2} \frac{\partial^2 x}{\partial t^2} + \frac{\alpha}{\rho} \frac{\partial x}{\partial t} - \nabla \cdot \left(\frac{1}{\rho} \nabla x \right) = \frac{f}{\rho}, \quad (1a)$$

with initial conditions

$$x = 0, \quad \frac{\partial x}{\partial t} = 0, \quad \text{for } t = 0, \quad \forall \boldsymbol{p} \in \Omega, \quad (1b)$$

and boundary constraints

$$x = 0, \qquad \forall t \in \mathbb{R}^+, \forall \boldsymbol{p} \in \Gamma_U,$$
$$\nabla x \cdot \boldsymbol{n}_D = 0, \quad \forall t \in \mathbb{R}^+, \forall \boldsymbol{p} \in \Gamma_D. \qquad (1c)$$

The forcing term is null in the absence of source and modeled as $f(\boldsymbol{p}, t; \boldsymbol{p}^s(t)) = s(t)\, \delta\left(\boldsymbol{p} - \boldsymbol{p}^s(t)\right)$ otherwise, where $s(t)$ is the source temporal waveform and δ denotes the Dirac delta. In this work, the function $s(t)$ is considered known, while the source position $\boldsymbol{p}^s(t)$ and the acoustic perturbation $x(\boldsymbol{p}, t; \boldsymbol{p}^s(t))$

TABLE I: Notation and symbols.

notation	description
$\mathbb{R}^+$	set of nonnegative real numbers
$\mathbb{N}^+$	set of nonnegative integers
$\mathcal{G}(\cdot; \mathbf{m}, \mathbf{P})$	Gaussian probability density with mean $\mathbf{m}$ and covariance $\mathbf{P}$
$\mathbf{a} \sim \mathcal{G}(\cdot; \mathbf{m}, \mathbf{P})$	$\mathbf{a}$ is Gaussian with mean $\mathbf{m}$ and covariance $\mathbf{P}$
$[\mathbf{a}; \mathbf{b}]$	$\begin{bmatrix} \mathbf{a} \\ \mathbf{b} \end{bmatrix}$
$col\,\{\mathbf{a}_i\}_{i=1}^N$	$[\mathbf{a}_1; \mathbf{a}_2; \ldots; \mathbf{a}_N]$
∇	$[\partial/\partial\xi; \partial/\partial\zeta]$
$\delta(\cdot)$	Dirac delta
$O(\cdot)$	in the order of

symbol	description
Ω	physical domain
Γ_U, Γ_D	upper boundary, seabed
ξ, ζ	range, depth
$b(\xi)$	bathymetry
$\mathbf{p} = [\xi; \zeta]$	position
$\alpha(\mathbf{p}), c(\mathbf{p}), \rho(\mathbf{p})$	damping coefficient, speed of sound, water density
t	time
$\mathbf{p}^s(t)$	source position
$x(\mathbf{p}, t; \mathbf{p}^s(t))$	acoustic pressure field produced by source located at $\mathbf{p}^s(t)$
$y_i(t)$	measured pressure at hydrophone i
$\mathbf{p}_i^h$	position of hydrophone i
N_h	no. of hydrophones
$s(t)$	source waveform
f_s	source frequency
Ω_d	truncated domain
Γ_L, Γ_R	left, right boundary
ξ_{max}	range extent
$\mathbf{n}$	outward pointing unit normal to the boundary
N_e	no. of spectral elements
Ω_e	spectral element
$\overline{D}$	reference depth
$\overline{\xi}, \overline{\zeta}$	transformed range, depth
N_ξ, N_ζ	no. of horizontal, vertical elements
ΔL	element length
$\Lambda = [-1, 1]^2$	reference element
$\mathcal{T}_e : \Lambda \to \Omega_e$	coordinate transformation
$\mathfrak{g}$	no. of GLL points
$P_\mathfrak{g}(\cdot)$	Legendre polynomial of degree $\mathfrak{g} - 1$
Ξ_e, Ξ	local, global mesh
$\mathcal{L}_i(\cdot)$	Lagrange polynomial associated to node i
N_n	no. of nodes
$\Phi_j(\mathbf{p})$	basis function of node j
$\mathbf{M}, \mathbf{D}, \mathbf{K}$	mass, damping, stiffness matrix
$\mathbf{f}(t)$	forcing term
Δt	time integration step
k	discrete time
$\mathbf{C}$	measurement matrix
$\sigma_{w_1}, \sigma_{w_2}, \sigma_{w_3}, \sigma_v$	std. dev. of pressure, pressure derivative, source position, measurement noise
T	sampling interval
$\mathbf{x}_k, \dot{\mathbf{x}}_k, \mathbf{p}_k^s$	pressure, pressure derivative, source position state
$\mathbf{z}_k$	augmented state
μ_k^e	probability of mode e
$\pi_{ee'}$	transition prob. from mode e' to e
q	ensemble size
$\hat{e}_k$	estimated mode
$\hat{\mathbf{p}}_{k|k}^s$	estimated source position
t^0	data assimilation starting time
t^*	source detection time

are to be estimated. More specifically, the temporal envelope $s(t)$ is a sinusoidal waveform with known frequency f_s:

$$s(t) = \sin(2\pi f_s t). \tag{2}$$

This assumption is reasonable for narrow-band sources typically encountered in underwater applications.

The above-stated dynamic estimation problem is clearly infinite-dimensional. To make it numerically tractable, a finite-dimensional approximation of the solution $x(\boldsymbol{p}, t; \boldsymbol{p}^s(t))$, based on the spectral-element method, is introduced in the next section.

III. Spectral-element discretization and time integration

A. Computational domain and integral formulation

Problem (1) is solved numerically through the *spectral element method* (SEM) proposed in [18]–[21]. The infinite domain Ω is first truncated along the horizontal axis, as illustrated in Fig. 1. The resulting computational domain Ω_d is delimited by the piecewise closed line $\Gamma_U \cup \Gamma_R \cup \Gamma_D \cup \Gamma_L$, and spans the physical region of interest:

$$\Omega_d = \left\{ (\xi, \zeta) \in \mathbb{R}^2 : \xi \in [0, \xi_{\max}], \zeta \in [0, b(\xi)] \right\}. \tag{3}$$

Let $\boldsymbol{n}$ denote the outward pointing unit normal on the boundary of Ω_d. To ensure that the acoustic waves leave the domain without significant spurious reflections, the following radiation condition [1, Chapter 7] is applied to the left and right boundaries, Γ_L and Γ_R:

$$\frac{1}{\rho} \nabla x \cdot \boldsymbol{n} = -\frac{1}{\rho c} \frac{\partial x}{\partial t}, \qquad \forall t \in \mathbb{R}^+, \forall \boldsymbol{p} \in \Gamma_L, \Gamma_R. \tag{4}$$

As highlighted by Jensen *et al.*, [1, Chapter 7], this constraint is only exact for a plane wave impinging normally onto a plane boundary. Nonetheless, it significantly reduces the amplitude of the numerical reflections even for moderate angles of incidence.

As a standard finite-element method, SEM is based on an integral formulation of problem (1). Multiplying (1a) by a generic space-dependent test function $\psi(\boldsymbol{p})$, integrating over Ω_d, and enforcing the boundary constraints (1c) and the radiation condition (4) yield

$$\frac{d^2}{dt^2} \int_{\Omega_d} \frac{\psi x}{\rho c^2} \, d\boldsymbol{p} + \frac{d}{dt} \int_{\Omega_d} \frac{\alpha \psi x}{\rho} \, d\boldsymbol{p} + \int_{\Omega_d} \frac{\nabla \psi \cdot \nabla x}{\rho} d\boldsymbol{p}$$

$$- \int_{\Omega_d} \frac{\psi f}{\rho} \, d\boldsymbol{p} - \int_{\Gamma_U} \frac{\psi \nabla x \cdot \boldsymbol{n}}{\rho} \, d\boldsymbol{p} + \frac{1}{\rho c}\bigg|_{\Gamma_L} \frac{d}{dt} \int_{\Gamma_L} \psi x \, d\boldsymbol{p}$$

$$+ \frac{1}{\rho c}\bigg|_{\Gamma_R} \frac{d}{dt} \int_{\Gamma_R} \psi x \, d\boldsymbol{p} = 0. \tag{5}$$

B. Computational mesh

The computational frame Ω_d (see Fig. 2)) is partitioned into a set of N_e non-overlapping quadrilateral elements Ω_e, $e = 1, \ldots, N_e$, such that

$$\Omega_d = \bigcup_{e=1}^{N_e} \Omega_e. \tag{6}$$

These elements are constructed with curvilinear boundaries to adapt to the irregular bottom. To this end, the following change of coordinates is first introduced:

$$\begin{aligned} \xi &= \bar{\xi}, \\ \zeta &= \frac{b(\bar{\xi})}{\bar{D}} \bar{\zeta}. \end{aligned} \tag{7}$$

In (7), the parameter $\bar{D}$ represents a characteristic reference depth. As a result, the complex waveguide Ω_d in the physical plane $O\xi\zeta$ is transformed into a rectangle $\bar{\Omega}_d$ in the plane $O\bar{\xi}\bar{\zeta}$:

$$\bar{\Omega}_d = \left\{ (\bar{\xi}, \bar{\zeta}) \in \mathbb{R}^2 : \bar{\xi} \in [0, \xi_{\max}], \bar{\zeta} \in [0, \bar{D}] \right\}. \tag{8}$$

The rectangular domain $\bar{\Omega}_d$ is then divided into N_e equal square elements $\bar{\Omega}_e$ with side ΔL, each of which corresponds to a curvilinear element Ω_e in the physical plane $O\xi\zeta$. Let N_ξ and N_ζ be the numbers of elements along the $\bar{\xi}$ and $\bar{\zeta}$ directions, respectively, so that $N_e = N_\xi \cdot N_\zeta$. Let $(\bar{\xi}_e, \bar{\zeta}_e)$ be the coordinates of the $e-$th element's center in the plane $O\bar{\xi}\bar{\zeta}$, and let $u, v \in [-1, 1]$ be local variables such that

$$\begin{aligned} \bar{\xi} &= \bar{\xi}_e + \frac{\Delta L}{2} u, \\ \bar{\zeta} &= \bar{\zeta}_e + \frac{\Delta L}{2} v. \end{aligned} \tag{9}$$

Each element Ω_e in the physical plane $O\xi\zeta$ is thus mapped to the reference square $\Lambda = [-1, 1] \times [-1, 1]$ (cf. Fig. 2):

$$\Lambda = \left\{ (u, v) \in \mathbb{R}^2 : u \in [-1, 1], v \in [-1, 1] \right\}. \tag{10}$$

Equations (7) and (9) define a local vector-valued invertible function $\mathcal{T}_e : \Lambda \to \Omega_e$ that maps the pair $(u, v) \in \Lambda$ to a point $\boldsymbol{p} \in \Omega_e$, i.e., $\boldsymbol{p} = \mathcal{T}_e(u, v)$.

For the sake of clarity, it is worth pointing out that the change of variables here employed to transform the irregular physical region into a rectangular domain allows to avoid using mesh generation software and dramatically simplifies the structure of the numerical solver. Nevertheless, such a change of variables is not strictly necessary, and unstructured meshes could be used to handle irregular seabeds.

C. Polynomial approximation in spectral elements

In a traditional finite-element method, low-degree polynomials are used as basis functions for computing the unknown field $x(\boldsymbol{p}, t)$. In the SEM, the pressure $x(\boldsymbol{p}, t)$ is approximated by a higher-degree Lagrangian interpolant. To this purpose, a set of $\mathfrak{g}$ nodes, called *Gauss-Lobatto-Legendre* (GLL) points, is first defined along each direction u, v, within the reference element Λ (cf. Fig. 2). On a direction $w = u, v$, the GLL nodes w_i, $i = 1, \ldots, \mathfrak{g}$, are defined as the roots of the equation

$$(1 - w^2) P'_{\mathfrak{g}}(w) = 0, \qquad w \in [-1, 1], \tag{11}$$

where $P'_{\mathfrak{g}}$ represents the first derivative of the Legendre polynomial of degree $\mathfrak{g} - 1$. Typically, $\mathfrak{g}$ is between 4 and 10. The GLL points are computed numerically and, as shown

in Fig. 2, they form a non-uniform grid of $\mathfrak{g} \times \mathfrak{g}$ nodes in Λ that is mapped, via $\mathcal{T}_e$, to a non-uniform grid Ξ_e in Ω_e:

$$
\begin{aligned}
\Xi_e = \{ \mathcal{T}_e(u_{i_u}, v_{i_v}); \ i_u, i_v = 1, \dots, \mathfrak{g} : \\
u_{i_u}, v_{i_v} \ \text{are solutions of (11)} \}.
\end{aligned}
\tag{12}
$$

Within a generic element Ω_e, the restriction $x^e(\boldsymbol{p}, t)$ of the pressure field $x(\boldsymbol{p}, t)$ to Ω_e is then approximated as

$$
x^e(\boldsymbol{p} = \mathcal{T}_e(u, v), t) \simeq \sum_{i_u = 1}^{\mathfrak{g}} \sum_{i_v = 1}^{\mathfrak{g}} \mathcal{L}_{i_u}(u) \, \mathcal{L}_{i_v}(v) \, x_{i_u i_v}^e(t), \tag{13}
$$

where $x_{i_u i_v}^e(t)$ is the time-dependent value of $x^e(\boldsymbol{p}, t)$ at the GLL point $\boldsymbol{p} = \mathcal{T}_e(u_{i_u}, v_{i_v})$ and $\mathcal{L}_i$ is the $\mathfrak{g}$−th degree Lagrange interpolating polynomial associated with node i, *i.e.*

$$
\mathcal{L}_i(w) = \prod_{\substack{\ell = 1 \\ \ell \neq i}}^{\mathfrak{g}} \frac{w - w_l}{w_i - w_l}. \tag{14}
$$

By definition, the function $\mathcal{L}_i(w)$ satisfies the property

$$
\mathcal{L}_i(w_j) = \begin{cases} 1, & i = j \\ 0, & \text{otherwise}. \end{cases} \tag{15}
$$

Boundary nodes are shared by neighbour elements, and the union of all local grids

$$
\Xi = \bigcup_{e=1}^{N_e} \Xi_e, \tag{16}
$$

contains

$$
N_n = [N_\xi(\mathfrak{g} - 1) + 1] \cdot [N_\zeta(\mathfrak{g} - 1) + 1] \tag{17}
$$

grid points $\boldsymbol{p}_j$, $j = 1, \dots, N_n$, that span the whole computational domain Ω_d. The triple of indices (e, i_u, i_v), with $i_u, i_v = 1, \dots, \mathfrak{g}$, identifies a unique node j of the global grid Ξ. As a result, the pressure field $x(\boldsymbol{p}, t)$ can be expressed as a linear combination of N_n spatially-varying basis functions $\Phi_j(\boldsymbol{p})$, $j = 1, \dots, N_n$, each of which is associated with a grid point j of Ξ. Accordingly, (13) is rewritten as

$$
x(\boldsymbol{p}, t) \simeq \sum_{j=1}^{N_n} \Phi_j(\boldsymbol{p}) \, x_j(t) = \boldsymbol{\Phi}^T(\boldsymbol{p}) \, \boldsymbol{x}(t), \tag{18}
$$

where $x_j(t)$ is the time-dependent value of the pressure field x at node j, and $\boldsymbol{\Phi}(\boldsymbol{p}), \boldsymbol{x}(t) \in \mathbb{R}^{N_n}$ are the column vectors

$$
\boldsymbol{\Phi}(\boldsymbol{p}) \triangleq \text{col}\{\Phi_j(\boldsymbol{p})\}_{j=1}^{N_n}, \quad \boldsymbol{x}(t) \triangleq \text{col}\{x_j(t)\}_{j=1}^{N_n}. \tag{19}
$$

The basis function $\Phi_j(\boldsymbol{p})$ does not vanish only at points $\boldsymbol{p}$ belonging to elements that contain the node j (more than one in the case of boundary nodes). More specifically, they are defined as

$$
\Phi_j(\boldsymbol{p}) = \begin{cases} \mathcal{L}_{i_u}(u) \, \mathcal{L}_{i_v}(v), & \boldsymbol{p} = \mathcal{T}_e(u, v) \in \Omega_e, \, \boldsymbol{p}_j \in \Xi_e \\[2mm] 0, & \boldsymbol{p} \notin \Omega_e. \end{cases} \tag{20}
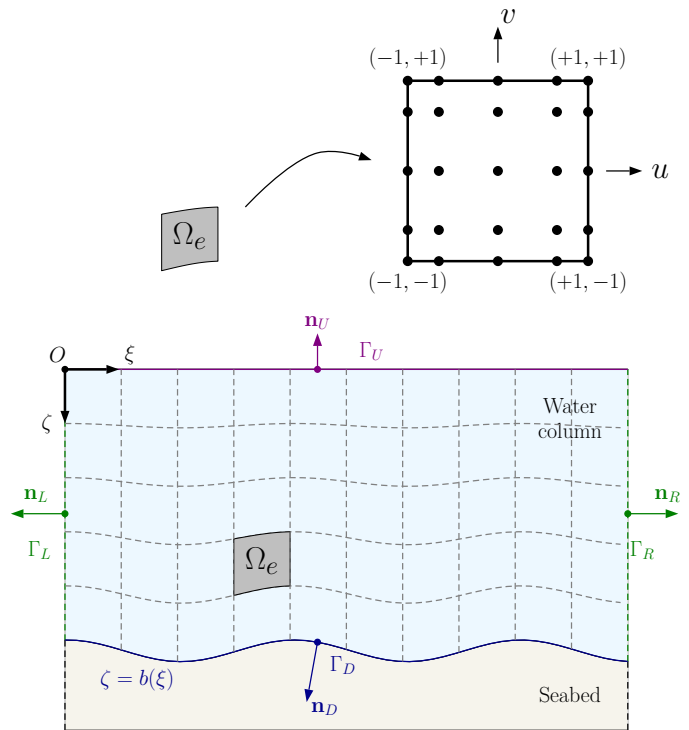$$

Fig. 2: Computational mesh, reference element Λ, and Gauss-Lobatto-Legendre (GLL) points for $\mathfrak{g} = 5$.

D. Time integration

To compute the N_n unknowns x_j, $j = 1, \dots, N_n$, expansion (18) is first introduced in the weak form (5). Then, by replacing the generic test function ψ with the basis functions, the following system of N_n second-order-in-time ordinary differential equations is obtained:

$$
\mathbf{M}\ddot{\boldsymbol{x}}(t) + \mathbf{D}\dot{\boldsymbol{x}}(t) + \mathbf{K}\boldsymbol{x}(t) - \boldsymbol{f}(t) = \mathbf{0}. \tag{21}
$$

In (21), $\mathbf{M}, \mathbf{D}, \mathbf{K} \in \mathbb{R}^{N_n \times N_n}$ are respectively the *mass*, *damping*, *stiffness* matrices, and $\boldsymbol{f}(t) \in \mathbb{R}^{N_n}$ is the forcing term defined as follows:

$$
\begin{aligned}
\mathbf{M} & \triangleq \int_\Omega \frac{\boldsymbol{\Phi}(\boldsymbol{p})\boldsymbol{\Phi}^T(\boldsymbol{p})}{\rho(\boldsymbol{p})c^2(\boldsymbol{p})} d\boldsymbol{p}, \\[2mm]
\mathbf{D} & \triangleq \int_\Omega \frac{\alpha(\boldsymbol{p})\boldsymbol{\Phi}(\boldsymbol{p})\boldsymbol{\Phi}^T(\boldsymbol{p})}{\rho(\boldsymbol{p})} d\boldsymbol{p} \\[2mm]
& + \left. \frac{1}{\rho c} \right|_{\boldsymbol{p} \in \Gamma_L} \int_{\Gamma_L} \boldsymbol{\Phi}(\boldsymbol{p})\boldsymbol{\Phi}^T(\boldsymbol{p}) \, d\boldsymbol{p} \\[2mm]
& + \left. \frac{1}{\rho c} \right|_{\boldsymbol{p} \in \Gamma_R} \int_{\Gamma_R} \boldsymbol{\Phi}(\boldsymbol{p})\boldsymbol{\Phi}^T(\boldsymbol{p}) \, d\boldsymbol{p}, \\[2mm]
\mathbf{K} & \triangleq \int_\Omega \frac{\nabla\boldsymbol{\Phi}(\boldsymbol{p}) \cdot (\nabla\boldsymbol{\Phi}(\boldsymbol{p}))^T}{\rho(\boldsymbol{p})} d\boldsymbol{p}, \\[2mm]
\boldsymbol{f}(t) & \triangleq s(t)\int_\Omega \frac{\boldsymbol{\Phi}(\boldsymbol{p})\delta(\boldsymbol{p} - \boldsymbol{p}^s)}{\rho(\boldsymbol{p})} d\boldsymbol{p} = \frac{s(t)\boldsymbol{\Phi}(\boldsymbol{p}^s)}{\rho(\boldsymbol{p}^s)}.
\end{aligned}
\tag{22}
$$

Integrals in (22) are evaluated through the GLL quadrature method [34]. In conjunction with the use of Lagrangian inter-

polants based on GLL nodes, this choice leads by construction to a diagonal mass matrix, which results into a drastic reduction of both the complexity of the numerical method and the computational time. No costly matrix inversion algorithm is indeed needed to compute the solution in time. This is one of the main differences between the SEM employed in this work and more classical FEMs.

Time discretization of (21) is achieved via an explicit Newmark scheme [18]. Let Δt be the time integration step. Then, the approximations $\boldsymbol{x}_{k+1}$ and $\dot{\boldsymbol{x}}_{k+1}$ at instant $t_{k+1} = (k+1)\Delta t$, $k \in \mathbb{N}^+$, of $\boldsymbol{x}$ and its time derivative $\dot{\boldsymbol{x}}$ are computed as

$$
\begin{aligned}
\boldsymbol{x}_{k+1} &= \boldsymbol{x}_k + \Delta t\, \dot{\boldsymbol{x}}_k + \frac{\Delta t^2}{2}\ddot{\boldsymbol{x}}_k, \\
\dot{\boldsymbol{x}}_{k+1} &= \dot{\boldsymbol{x}}_k + \frac{\Delta t}{2}\left(\ddot{\boldsymbol{x}}_k + \ddot{\boldsymbol{x}}_{k+1}\right),
\end{aligned} \tag{23}
$$

with the initial conditions

$$
\boldsymbol{x}_0 = \dot{\boldsymbol{x}}_0 = \boldsymbol{0}. \tag{24}
$$

Using (21) for $\ddot{\boldsymbol{x}}_k$ and $\ddot{\boldsymbol{x}}_{k+1}$ finally yields the following discrete-time linear system

$$
\begin{aligned}
\boldsymbol{x}_{k+1} &= \boldsymbol{x}_k + \Delta t\, \dot{\boldsymbol{x}}_k + \frac{\Delta t^2}{2}\Big[-\mathbf{M}^{-1}\mathbf{D}\dot{\boldsymbol{x}}_k \\
&\quad - \mathbf{M}^{-1}\mathbf{K}\boldsymbol{x}_k + \mathbf{M}^{-1}\boldsymbol{f}_k\Big],
\end{aligned} \tag{25a}
$$

$$
\begin{aligned}
\dot{\boldsymbol{x}}_{k+1} &= \left[\mathbf{I} + \frac{\Delta t}{2}\mathbf{M}^{-1}\mathbf{D}\right]^{-1}\left[\left(\mathbf{I} - \frac{\Delta t}{2}\mathbf{M}^{-1}\mathbf{D}\right)\dot{\boldsymbol{x}}_k \right. \\
&\quad + \frac{\Delta t}{2}\left(-\mathbf{M}^{-1}\mathbf{K}\boldsymbol{x}_k + \mathbf{M}^{-1}\boldsymbol{f}_k \right. \\
&\quad \left.\left. - \mathbf{M}^{-1}\mathbf{K}\boldsymbol{x}_{k+1} + \mathbf{M}^{-1}\boldsymbol{f}_{k+1}\right)\right],
\end{aligned} \tag{25b}
$$

where $\boldsymbol{f}_k \triangleq \boldsymbol{f}(t_k) = s(t_k)\,\rho^{-1}(\boldsymbol{p}^s(t_k))\,\boldsymbol{\Phi}(\boldsymbol{p}^s(t_k))$. Equations (25) are solved sequentially: the discretized acoustic pressure $\boldsymbol{x}_{k+1}$ is first computed via (25a) and is then inserted in (25b) to calculate its derivative $\dot{\boldsymbol{x}}_{k+1}$.

To conclude, at each time instant $t_k = k\,\Delta t$, $k \in \mathbb{N}^+$, the pressure signals $\boldsymbol{x}_k^h \triangleq \mathrm{col}\{x(\boldsymbol{p}_i^h, t_k)\}_{i=1}^{N_h}$ measured by the hydrophones at locations $\boldsymbol{p}_i^h$, $i = 1, \ldots, N_h$, are given by

$$
\boldsymbol{x}_k^h = \boldsymbol{C}\boldsymbol{x}_k, \tag{26}
$$

where the elements of the $N_h \times N_n$ matrix $\boldsymbol{C}$ turn out to be

$$
C_{ij} = \Phi_j(\boldsymbol{p}_i^h), \quad i = 1, \ldots, N_h, \quad j = 1, \ldots, N_n. \tag{27}
$$

IV. SOURCE DETECTION AND LOCALIZATION

A. Multiple Model Approach

Relying on the SEM of the previous section, the key idea for source detection and localization pursued in this work is to consider multiple hypotheses, one corresponding to the absence of the source and the others corresponding to a source located in a generic element of the SE mesh. In this way, recalling that the source presence/location only affects the

forcing term $\boldsymbol{f}_k = \boldsymbol{f}(t_k)$ in (25), it is possible to associate an appropriate model to each hypothesis and adopt a multiple-model filtering approach [35, chapter 11] in order to ascertain which model/hypothesis is more likely with the available sensor measurements and accordingly decide whether the source is present (detection) and, in such a case, estimate its position (localization).

To be more precise, let $\mathcal{N}_e \subset \{1, \ldots, N_n\}$ denote the subset of nodes of element $e \in \{1, \ldots, N_e\}$ and let $e = 0$ refer to the null model/hyphotesis accounting for the absence of the source in the monitored area. Then, for model/hypothesis $e \in \{1, \ldots, N_e\}$, the forcing term $\boldsymbol{f}_k = \boldsymbol{f}_k^e$ turns out to be

$$
\boldsymbol{f}_k^e = s_k\,\rho^{-1}(\boldsymbol{p}_k^s)\,\boldsymbol{\Phi}^e(\boldsymbol{p}_k^s), \quad e = 1, \ldots, N_e \tag{28}
$$

where

$$
\begin{aligned}
\boldsymbol{\Phi}^e(\boldsymbol{p}) &\triangleq \mathrm{col}\{\Phi_j^e(\boldsymbol{p})\}_{j=1}^{N_n} \\
\Phi_j^e(\boldsymbol{p}) &= \begin{cases} \Phi_j(\boldsymbol{p}), & j \in \mathcal{N}_e \\ 0, & j \notin \mathcal{N}_e \end{cases}
\end{aligned} \tag{29}
$$

is the restriction of $\boldsymbol{\Phi}(\boldsymbol{p})$ to element e for $e = 1, \ldots, N_e$ (source located in Ω_e), while for $e = 0$ (non-existing source) $\boldsymbol{f}_k^e$ is null. Accordingly, the model matched to hypothesis $e \in \{0, 1, \ldots, N_e\}$ consists of the following state equations for acoustic pressure $\boldsymbol{x}_k$ and its derivative $\dot{\boldsymbol{x}}_k$

$$
\begin{aligned}
\boldsymbol{x}_{k+1} &= \boldsymbol{x}_k + \Delta t\, \dot{\boldsymbol{x}}_k + \frac{\Delta t^2}{2}\Big[-\mathbf{M}^{-1}\mathbf{D}\dot{\boldsymbol{x}}_k \\
&\quad - \mathbf{M}^{-1}\mathbf{K}\boldsymbol{x}_k + \mathbf{M}^{-1}\boldsymbol{f}_k^e\Big] + \boldsymbol{w}_{1,k},
\end{aligned} \tag{30a}
$$

$$
\begin{aligned}
\dot{\boldsymbol{x}}_{k+1} &= \left[\mathbf{I} + \frac{\Delta t}{2}\mathbf{M}^{-1}\mathbf{D}\right]^{-1}\left[\left(\mathbf{I} - \frac{\Delta t}{2}\mathbf{M}^{-1}\mathbf{D}\right)\dot{\boldsymbol{x}}_k \right. \\
&\quad + \frac{\Delta t}{2}\left(-\mathbf{M}^{-1}\mathbf{K}\boldsymbol{x}_k + \mathbf{M}^{-1}\boldsymbol{f}_k^e \right. \\
&\quad \left.\left. - \mathbf{M}^{-1}\mathbf{K}\boldsymbol{x}_{k+1} + \mathbf{M}^{-1}\boldsymbol{f}_{k+1}^e\right)\right] + \boldsymbol{w}_{2,k},
\end{aligned} \tag{30b}
$$

Further, whenever $e \neq 0$ (existing source located in Ω_e), the dynamical model for the source position $\boldsymbol{p}_k^s$ is

$$
\boldsymbol{p}_{k+1}^s = \boldsymbol{p}_k^s + \boldsymbol{w}_{3,k}. \tag{30c}
$$

In (30), $\boldsymbol{w}_{1,k}, \boldsymbol{w}_{2,k}, \boldsymbol{w}_{3,k}$ are process disturbances that account for uncertainty on pressure, pressure derivative, and source position, respectively. Such process disturbances can be used to account for different sources of uncertainty including parameter uncertainties, time and space discretization errors, etc.. Note that in (30c) the position of the source is assumed to vary slowly with time and, hence, to follow a discrete-time random walk.

Then, each of the above models involves the augmented state

$$
\boldsymbol{z}_k = \begin{cases} [\boldsymbol{x}_k; \dot{\boldsymbol{x}}_k] \in \mathbb{R}^{2N_n}, & e = 0 \\ [\boldsymbol{x}_k; \dot{\boldsymbol{x}}_k; \boldsymbol{p}_k^s] \in \mathbb{R}^{2(N_n+1)}, & e = 1, \ldots, N_e. \end{cases} \tag{31}
$$

In view of (26), the measurement equation turns out to be independent from e equal to

$$\boldsymbol{y}_k = \boldsymbol{C}\boldsymbol{x}_k + \boldsymbol{v}_k \tag{32}$$

where $\boldsymbol{y_k}$ is the vector of all measurements collected from the sensor array and $\boldsymbol{v}_k$ accounts for measurement noise.

The multiple-model filter for source detection and localization runs a bank of $N_e + 1$ spectral-element nonlinear filters associated to the above discussed hypotheses ($e = 0$ for source absence and $e = 1, \ldots, N_e$ for its presence in spectral-element e). To this end, each filter e must propagate in time predicted (filtered) estimates $\hat{\boldsymbol{z}}_{k|k-1}^e$ ($\hat{\boldsymbol{z}}_{k|k}^e$) of the augmented state $\boldsymbol{z}_k$ defined in (31) according to hypothesis e, along with the probability

$$\mu_k^e = Prob\left(e_k = e\right) \tag{33}$$

that the current mode e_k is equal to hypothesis e. Transitions among hypotheses are modeled, as usual, by means of a homogeneous Markov chain with constant transition probabilities

$$\pi_{ee'} = Prob\left(e_k = e | e_{k-1} = e'\right). \tag{34}$$

Remark 1 - The choice of the above transition probabilities could be related to the ratio $r = T/\tau_{min}$ of the filter sampling interval T to the minimum sojourn time $\tau_{min} = \frac{\Delta L}{v_{max}}$ of the source within an SE, v_{max} denoting the maximum source speed. In fact such ratio, satisfying $r < 1$ for typical values of $(\Delta L, v_{max}, T)$, can be regarded as a probability that the source leaves an element e' to enter a neighboring element e; hence r should be equally divided among all neighbors e of e' to define $\pi_{ee'}$ and the residual probability be assigned to permanence in e', i.e. $\pi_{e'e'} = 1 - r$. In particular, if the source is known to be motionless (infinite sojourn time), the suggested choice is $\pi_{ee'} = 1$ for $e = e'$ or $\pi_{ee'} = 0$ otherwise.

Remark 2 - Tracking of a quickly moving source could be accomplished in the multiple model framework by: 1) adopting suitable higher-order kinematic models in place of the random-walk model (30c), 2) suitably specifying the transition probabilities in (34), and 3) resorting to an *interacting multiple model* (IMM) approach [35]. It is worth to point out, however, that the standard IMM filter involves mixing of the multiple model states and needs therefore to be tailored to the source tracking case where the source states of the various models, constrained to belong to different spectral elements, cannot clearly be mixed. The extension of this approach to the case of a moving source will be objective of future work.

B. Ensemble Kalman Filter

The critical point of this approach is that the state $\boldsymbol{z}_k$ in (31) tends to be of very high dimension since it is in the order of $2N_n$. In fact, from (17) it turns out that $N_n = N_\xi N_\zeta \mathfrak{g}^2 + \cdots$ is in the order of $N_e \mathfrak{g}^2$, where $N_e = N_\xi N_\zeta$ is the number of elements of the mesh and $\mathfrak{g}$ the number of nodes along each side of the SE, and hence is typically very large especially when the size of the computational domain Ω_d increases and/or the mesh resolution ΔL gets finer and/or $\mathfrak{g}$ increases. In this respect, the cubic computational complexity and quadratic memory complexity (with respect to the state dimension

n) of any Kalman-like filter propagating in time the state covariance matrix, would become infeasible. To this end, the so called *ensemble Kalman filter* (EnKF) has been devised [32], [36] to efficiently cope with problems (e.g., in meteorology, geoscience, oceanography) that involve a large number of state variables typically arising from spatial discretizations of partial differential equations. The idea of EnKF is to replace the $n \times n$ state covariance matrix (where n is the dimension of the state vector) with an ensemble consisting of randomly sampled $q \ll n$ state vectors and to compute the required statistics for estimation (mean, cross-covariance between state and measurement, measurement covariance) as sample averages over the ensemble. This allows to drop the computational complexity from $O(n^3)$ to $O(n^2 q)$ and the memory complexity from $O(n^2)$ to $O(nq)$ see [38, section 4.2]), with significant savings provided that the ensemble size q is much smaller than the state dimension n.

The pseudo-code of a *multiple-model spectral-element EnKF* (MM-SE-EnKF) for acoustic source detection and localization is provided in Algorithm 1. Such algorithm consists of the following steps.

1) **Prediction**: first, for each element hypothesis e and member of the ensemble i, the acoustic pressure field is predicted by the space-time discretized acoustic wave propagation model (30a)-(30b) and, if $e \neq 0$, the source position is also predicted by the random walk model (30c); then, mode probabilities are predicted by the Markov chain transition model (34).

2) **Correction**: the augmented states, for any e and i, and mode probabilities, for any e, are corrected on the basis of the available measurements from hydrophones.

3) **Source detection & localization**: the hypothesis e with highest probability is selected and, if $e \neq 0$ (detected source), the source is localized according to the corrected source position relative to such hypothesis.

MM-SE-EnKF runs a bank of $N_e + 1$ SE-EnKFs each associated to a possible hypothesis (mode) $e \in \{0, 1, \ldots, N_e\}$ and propagating in time predicted and filtered augmented state estimates $\hat{z}_{k|k-1}^e$ and, respectively, $\hat{z}_{k|k}^e$ as well as the mode probability μ_k^e. Each filter can run independently of the others performing, at each time k, the prediction step (lines 4-25 of the pseudo-code) followed by the correction step (lines 26-47) and by the source detection & localization step (lines 48-58). Notice that each mode-matched SE-EnKF employs an ensemble of size q to compute the required joint statistics for the augmented state $\boldsymbol{z}$ and measurement $\boldsymbol{y}$ (lines 22, 33 and 34).

Notice also that, in each EnKF, the model uncertainties are incorporated through the use of ensemble simulations to generate multiple realizations of the state vector in the prediction step to approximate the underlying probability distribution. Such model uncertainties are quantified in terms of the variances $\sigma_{w_1}^2, \sigma_{w_2}^2, \sigma_{w_3}^2$ of the process disturbances $\boldsymbol{w}_{1,k}, \boldsymbol{w}_{2,k}, \boldsymbol{w}_{3,k}$ which determine the spread of the ensemble simulations.
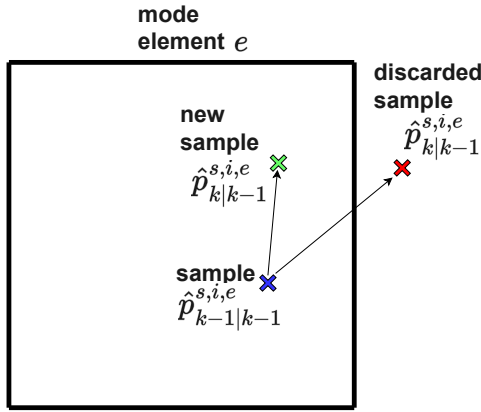
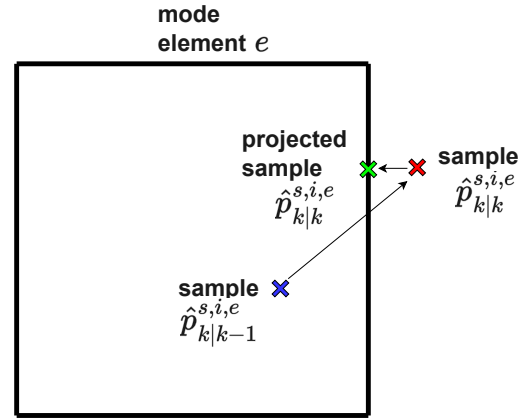Fig. 3: Resampling for contraint enforcement in the prediction step.

Fig. 4: Projection for constraint enforcement in the correction step.

C. Constraints in prediction and correction steps

Recalling that filter e, for $e > 0$, is associated to the hypothesis that the source is located in Ω_e, then the source position samples $\hat{\boldsymbol{p}}_{k|k-1}^{s,i,e}$ and $\hat{\boldsymbol{p}}_{k|k}^{s,i,e}$ must be enforced to be in Ω_e.

This can be accomplished in several different ways. For the sake of computational simplicity, in this paper we adopt the following procedure.

- In the prediction step, $\hat{\boldsymbol{p}}_{k|k-1}^{s,i,e}$ is resampled until if falls inside Ω_e (see Fig. 4).
- In the correction step, any sample $\hat{\boldsymbol{p}}_{k|k}^{s,i,e}$ falling outside Ω_e is projected to the closest point on the boundary of Ω_e (see Fig. 5).

The reason for this different handling of constraint violation in prediction and correction steps can be explained as follows. For source location prediction

$$\hat{\boldsymbol{p}}_{k|k-1}^{s,i,e} = \hat{\boldsymbol{p}}_{k-1|k-1}^{s,i,e} + \boldsymbol{w}_{3,k-1}^{i,e},$$

starting from $\hat{\boldsymbol{p}}_{k-1|k-1}^{s,i,e} \in \Omega_e$ and provided that σ_{w_3} is sufficiently small compared to the element size ΔL, it is quite unlikely that $\hat{\boldsymbol{p}}_{k|k-1}^{s,i,e} \notin \Omega_e$ for several consecutive draws of $\boldsymbol{w}_{3,k-1}^{i,e} \sim \mathcal{G}\left(\cdot; \boldsymbol{0}, \sigma_{w_3}^2 \boldsymbol{I}\right)$; hence, in this case, resampling represents a simple and effective solution. On the other hand, correction (line 37) tends to push $\hat{\boldsymbol{p}}_{k|k}^{s,i,e}$ outside Ω_e for elements e that are far away from the true source position; in such a case, resampling would be highly inefficient while projection onto the element boundary is a simple and efficient solution.

D. Computational complexity of MM-SE-EnKF

It is first worth pointing out that the computational burden of MM-SE-EnKF is mostly due to the $N_e + 1$ mode-matched filters, as the remaining part (lines 48-56) involves a negligible amount of computation. Moreover, such filters can clearly run in parallel so that they can be assigned to N_p processors roughly reducing the overall computational load of a factor N_p.

Hence, hereafter the focus is on the computational complexity of the single SE-EnKF (lines 6-46). Recalling that $N_n \geq N_e \mathfrak{g}^2 \geq N_e$ and that the ensemble size q must be chosen

such that $N_h \leq q \ll N_n$ for the sake of computational reduction as well as to guarantee that the $N_h \times N_h$ matrix $\boldsymbol{P}_{y,k}^e$ computed in line 33 of algorithm 1 be invertible, the most burdensome task of SE-EnKF is for pressure and pressure derivative prediction which takes in the order of $N_n^2 q$ operations. Conversely, the correction step has $O(N_n q N_h)$ computational complexity required for the computation of matrix $\boldsymbol{P}_{zy,k}^e$ (line 34). Summing up, the overall computational complexity of MM-SE-EnKF turns out to be $O(N_n^2 N_e q)$. Assigning the various SE-EnKFs to $O(N_e)$ parallel processors it is clearly possible to reduce the processing time for a single recursion of MM-SE-EnKF to $O(N_n^2 q)$.

E. Fast MM-SE-EnKF

To further reduce the computational load and thus allow working at faster sampling rates, a computationally cheaper version of MM-SE-EnKF referred to as *fast MM-SE-EnKF* (FMM-SE-EnKF) has been devised (see the pseudocode of Algorithm 2) to deal with a motionless acoustic source possibly located in the surveillance area Ω_d.

FMM-SE-EnKF switches between two operating phases:

1) an initial *source detection* phase that aims to detect the presence of the source and single out the element Ω_e where it is located;
2) a *source localization* phase that aims to accurately localize the source within Ω_e.

The source detection phase must clearly take into account all possible hypotheses $e \in \{0, 1, \ldots, N_e\}$ but, for the sake of computational efficiency, each mode-matched filter only performs prediction (but not correction with the available sensor measurements) of the pressure field estimate (lines 5-6 of Algorithm 2) and exploits the measurements only to update the hypothesis probabilities μ_k^e (lines 7-9). This allows to drop the computational complexity from $O(N_n^2 N_e q)$ to $O(N_n^2 N_e)$ as no ensemble is required to compute the sample statistics for augmented state correction. In fact, prediction (25a)-(25b) involves multiplication of off-line computed $N_n \times N_n$ matrices by $N_n \times 1$ vectors for $N_e + 1$ models. Conversely, the subsequent source localization phase only needs to run a single SE-EnKF for the selected hypothesis $\hat{e}_k$ resulting from the source

---

Algorithm 1 - MM-SE-EnKF at time k

1: **Input:** $\left\{\mu_{k-1}^e\right\}_{e=0}^{N_e}, \left\{\hat{z}_{k-1|k-1}^{i,e}\right\}_{i=1,e=0}^{q,N_e}, \left\{\pi_{ee'}\right\}_{e,e'=0}^{N_e}$,

2: $\quad \sigma_{w_1}, \sigma_{w_2}, \sigma_{w_3}, \sigma_v, \boldsymbol{C}, N_e, q, \boldsymbol{y}_k$

3: **for** $e = 0, 1, \dots, N_e$ **do**

4: $\quad$ **PREDICTION:**

5: $\quad$ **for** $i = 1, 2, \dots, q$ **do**

6: $\quad\quad$ draw sample $\boldsymbol{w}_{1,k-1}^{i,e} \sim \mathcal{G}(\cdot; \boldsymbol{0}, \sigma_{w_1}^2 \boldsymbol{I})$

7: $\quad\quad$ compute predicted pressure sample $\hat{\boldsymbol{x}}_{k|k-1}^{i,e}$ by (30a)

8: $\quad\quad$ $\hat{\boldsymbol{y}}_k^{i,e} = \boldsymbol{C}\hat{\boldsymbol{x}}_{k|k-1}^{i,e}$

9: $\quad\quad$ draw sample $\boldsymbol{w}_{2,k-1}^{i,e} \sim \mathcal{G}(\cdot; \boldsymbol{0}, \sigma_{w_2}^2 \boldsymbol{I})$

10: $\quad\quad$ compute predicted pressure derivative $\hat{\dot{\boldsymbol{x}}}_{k|k-1}^{i,e}$ by (30b)

11: $\quad\quad$ $\hat{\boldsymbol{z}}_{k|k-1}^{i,e} = \left[\hat{\boldsymbol{x}}_{k|k-1}^{i,e}; \hat{\dot{\boldsymbol{x}}}_{k|k-1}^{i,e}\right]$

12: $\quad\quad$ **if** $e \neq 0$ **then**

13: $\quad\quad\quad$ **Repeat**

14: $\quad\quad\quad$ draw sample $\boldsymbol{w}_{3,k-1}^{i,e} \sim \mathcal{G}(\cdot; \boldsymbol{0}, \sigma_{w_3}^2 \boldsymbol{I})$

15: $\quad\quad\quad$ compute predicted position sample $\hat{\boldsymbol{p}}_{k|k-1}^{s,i,e}$ by (30c)

16: $\quad\quad\quad$ **until** $\hat{\boldsymbol{p}}_{k|k-1}^{s,i,e} \in \Omega_e$

17: $\quad\quad\quad$ $\hat{\boldsymbol{z}}_{k|k-1}^{i,e} = \left[\hat{\boldsymbol{z}}_{k|k-1}^{i,e}; \hat{\boldsymbol{p}}_{k|k-1}^{s,i,e}\right]$

18: $\quad\quad$ **end if**

19: $\quad\quad$ predict mode probability as $\mu_{k|k-1}^e = \sum_{e'=0}^{N_E} \pi_{ee'}\, \mu_{k-1}^{e'}$

20: $\quad$ **end for**

21: $\quad$ compute predicted state and measurement:

22: $\quad\quad$ $\hat{\boldsymbol{z}}_{k|k-1}^e = q^{-1} \sum_{i=1}^q \hat{\boldsymbol{z}}_{k|k-1}^{i,e}$

23: $\quad\quad$ $\boldsymbol{E}_{z,k}^e = [\hat{\boldsymbol{z}}_{k|k-1}^{1,e} - \hat{\boldsymbol{z}}_{k|k-1}^e, \dots, \hat{\boldsymbol{z}}_{k|k-1}^{q,e} - \hat{\boldsymbol{z}}_{k|k-1}^e]$

24: $\quad\quad$ $\hat{\boldsymbol{y}}_k^e = q^{-1} \sum_{i=1}^q \hat{\boldsymbol{y}}_k^{i,e}$

25: $\quad\quad$ $\boldsymbol{E}_{y,k}^e = [\boldsymbol{y}_k - \hat{\boldsymbol{y}}_k^{1,e}, \dots, \boldsymbol{y}_k - \hat{\boldsymbol{y}}_k^{q,e}]$

26: $\quad$ **CORRECTION:**

27: $\quad$ compute ensemble sample covariances:

28: $\quad$ **for** $i = 1, 2, \dots, q$ **do**

29: $\quad\quad$ draw sample $\boldsymbol{v}_k^{i,e} \sim \mathcal{G}(\cdot; \boldsymbol{0}, \sigma_v^2 \boldsymbol{I})$

30: $\quad$ **end for**

31: $\quad$ $\boldsymbol{V}_k^e = [\boldsymbol{v}_k^{1,e}, \dots, \boldsymbol{v}_k^{q,e}]$

32: $\quad$ $\boldsymbol{R} = (q-1)^{-1}\, \boldsymbol{V}_k^e (\boldsymbol{V}_k^e)^T$

33: $\quad$ $\boldsymbol{P}_{y,k}^e = (q-1)^{-1} \boldsymbol{E}_{y,k}^e (\boldsymbol{E}_{y,k}^e)^T + \boldsymbol{R}$

34: $\quad$ $\boldsymbol{P}_{zy,k}^e = (q-1)^{-1} \boldsymbol{E}_{z,k}^e (\boldsymbol{E}_{y,k}^e)^T$

35: $\quad$ $\boldsymbol{L}_k^e = \boldsymbol{P}_{zy,k}^e\, (\boldsymbol{P}_{y,k}^e)^{-1}$

36: $\quad$ **for** $i = 1, 2, \dots, q$ **do**

37: $\quad\quad$ $\hat{\boldsymbol{z}}_{k|k}^{i,e} = \hat{\boldsymbol{z}}_{k|k-1}^{i,e} + \boldsymbol{L}_k^e \left(\boldsymbol{y}_k + \boldsymbol{v}_k^{i,e} - \hat{\boldsymbol{y}}_k^{i,e}\right)$

38: $\quad\quad$ **if** $e \neq 0$ **then**

39: $\quad\quad\quad$ position projection:

40: $\quad\quad\quad$ **if** $\hat{\boldsymbol{p}}_{k|k}^{s,i,e} \notin \Omega_e$ **then** project it to the closest point on

41: $\quad\quad\quad\quad$ the boundary of Ω_e, as shown in Fig. 4

42: $\quad\quad\quad$ **end if**

43: $\quad\quad$ **end if**

44: $\quad$ **end for**

45: $\quad$ compute likelihood as $\lambda_k^e = \mathcal{G}(\boldsymbol{y}_k; \hat{\boldsymbol{y}}_k^e, \boldsymbol{P}_{y,k}^e)$

46: $\quad$ update mode probability as $\mu_k^e = \lambda_k^e\, \mu_{k|k-1}^e$

47: **end for**

48: **SOURCE DETECTION & LOCALIZATION:**

49: find best mode:

50: $\quad$ $\hat{e}_k = \arg\max_e \mu_k^e$

51: normalize mode probabilities:

52: $\quad$ $c = \sum_{e'=0}^{N_e} \mu_k^{e'}$

53: $\quad$ $\mu_k^e = c^{-1} \mu_k^e \quad$ for $e = 0, 1, \dots, N_e$

54: **if** $\hat{e}_k \neq 0$ **then**

55: $\quad$ compute estimated position:

56: $\quad\quad$ $\hat{\boldsymbol{p}}_{k|k}^{s,i} = [\boldsymbol{0}\ \boldsymbol{I}_2]\, \hat{\boldsymbol{z}}_{k|k}^{i,\hat{e}_k}$ for $i = 1, \dots, q$

57: $\quad\quad$ $\hat{\boldsymbol{p}}_{k|k}^s = q^{-1} \sum_{i=1}^q \hat{\boldsymbol{p}}_{k|k}^{s,i}$

58: **end if**

Algorithm 2 - FMM-SE-EnKF at time k

1: **Input:** $\left\{\mu_{k-1}^e\right\}_{e=0}^{N_e}, \left\{\hat{z}_{k-1|k-1}^e\right\}_{e=0}^{N_e}, \left\{\pi_{ee'}\right\}_{e,e'=0}^{N_e}$,

2: $\quad \sigma_{w_1}, \sigma_{w_2}, \sigma_{w_3}, \sigma_v, \boldsymbol{R}_0 = \sigma_v^2 \boldsymbol{I}, \boldsymbol{C}, N_e, q, k_s > 1, \boldsymbol{y}_k$

3: **if** $\hat{k} \leq k_s$ **then**

4: $\quad$ **SOURCE DETECTION**

5: $\quad$ **for** $e = 0, 1, \dots, N_e$ **do**

6: $\quad\quad$ predict pressure $\hat{\boldsymbol{x}}_{k|k-1}^e$ and derivative $\hat{\dot{\boldsymbol{x}}}_{k|k-1}^e$ by

7: $\quad\quad$ (25) with source position fixed at the center of Ω_e

8: $\quad\quad$ $\hat{\boldsymbol{y}}_k^e = \boldsymbol{C}\hat{\boldsymbol{x}}_{k|k-1}^e$

9: $\quad\quad$ compute likelihood: $\lambda_k^e = \mathcal{G}(\boldsymbol{y_k}; \hat{\boldsymbol{y}}_k^e, \boldsymbol{R}_0)$

10: $\quad\quad$ update mode probabilities: $\mu_k^e = \lambda_k^e \sum_{h=0}^{N_e} \pi_{eh}\mu_{k-1}^h$

11: $\quad$ **end for**

12: $\quad$ find best mode: $\hat{e}_k = \arg\max_e \mu_k^e$

13: $\quad$ normalize mode probabilities:

14: $\quad$ $c = \sum_{h=0}^{N_e} \mu_k^h$

15: $\quad$ $\mu_k^e = c^{-1} \mu_k^e \quad$ for $e = 0, 1, \dots, N_e$

16: $\quad$ **if** $\hat{e}_k \neq 0$ **and** $\hat{e}_k = \hat{e}_{k-1}$ **then**

17: $\quad\quad$ $\hat{k} = \hat{k} + 1$

18: $\quad$ **else**

19: $\quad\quad$ $\hat{k} = 1$

20: $\quad$ **end if**

21: **else**

22: $\quad$ **SOURCE LOCALIZATION**

23: $\quad$ set $\hat{e}_k$ equal to $\hat{e}_{k-1}$

24: $\quad$ only for mode $\hat{e}_k$, run the SE-EnKF as described

25: $\quad$ in Algorithm 1

26: **end if**

---

detection phase; in this phase, the computational complexity is just $O(N_n^2 q)$, the complexity of a single EnKF with state dimension $2N_n + 2 = O(N_n)$ and ensemble size q. The switching from the initial detection phase to the localization phase can be performed either after a prescribed setup time or whenever the selected hypothesis $\hat{e}_k$ has remained unchanged for a sufficiently high number k_s of consecutive recursions in

the detection phase (see Algorithm 2 where the counter $\hat{k}$ is initialized to 1). Notice that Algorithm 2, wherein the selected hypothesis is held fixed after the switching, is appropriate for a static (i.e. motionless and always emitting) source but should clearly be reconceived for the dynamic source case which, however, is outside the scope of this paper and left for possible future work.

Regular seabed				
	N_e	N_n	$\mathfrak{g}$	ΔL [m]
ground-truth	5400	87683	5	5
filter	1350	22237	5	10
Irregular seabed				
	N_e	N_n	$\mathfrak{g}$	ΔL [m]
ground-truth	6000	97281	5	5
filter	1500	24641	5	10

TABLE II: Spectral-element mesh parameters for both ground-truth simulator and filter, in scenarios with regular and irregular seabed.

σ_{w_1} [mPa]	σ_{w_2} [Pa/s]	σ_{w_3} [m]	σ_v [Pa]
0.1	0.0628	0.001	0.05
T [ms]	q	π_{ee}	$\pi_{ee'},\ e \neq e'$
0.46	100	1	0

TABLE III: Parameters of FMM-SE-EnKF for both scenarios with regular and irregular seabed (T denotes the filter sampling interval).

V. SIMULATION RESULTS

We considered two scenarios to characterize the capabilities of the FMM-SE-EnKF algorithm. The first configuration, shown in Fig. 5, is used to assess the filter performance. The FMM-SE-EnKF algorithm is additionally compared to the *minimum variance, distortionless filter matched field processing* (MVDF-MFP) algorithm proposed by [10]. It is worth emphasizing that current implementations of the MFP are based on normal modes [1], [37] and are, by construction, applicable only in depth-dependent media with flat horizontal boundaries. On the contrary, the present algorithm can be employed in more general space-time-varying underwater environments involving complex boundaries. The second scenario, shown in Fig. 6, is therefore designed to show the FMM-SE-EnKF algorithm's performance in the case of a variable seabed.

A. Scenario with regular seabed

This first scenario, inspired by a benchmark used in [39], involves a motionless source emitting a signal of frequency $f_s = 100\,Hz$ for a total simulation time of $10\,s$ and time integration step $\Delta t = 0.23\,ms$. The source is located within a shallow water environment with an isospeed water column ($c = 1500\,m/s$, $\rho = 1000\,Kg/m^3$, $\alpha = 4 \cdot 10^{-6}\,s/m^2$) of $90\,m$ depth and $1500\,m$ length located at $\xi = 1212.5\,m$ and $\zeta = 57.5\,m$. Fig. 5 shows the source position $\boldsymbol{p}^s$ and the hydrophone positions $\boldsymbol{p}_i^h$, for $i = 1, \dots, N_h$, and provides a comparison between mesh elements $\Omega_{e,l}$ used by the ground-truth simulator with side length $l = \Delta L_g$, and by the filter with side length $l = \Delta L_f$ within the domain Ω_d. We set the *mesh size ratio* (MSR), defined as the ratio $\mathrm{MSR} \triangleq \Delta L_f/\Delta L_g$ between the side length of the mesh element used by the filter and the one used by the ground-truth simulator, to $\mathrm{MSR} = 0.5$. Mesh parameters of the ground-truth simulator and of the filter are reported in Table II. Filter parameters have been set as reported in Table III. The filter collects measurements from a *vertical array* (VA) of $N_h = 20$ hydrophones located $1\,Km$ away from the source in an environment with a *signal-to-noise ratio* (SNR) of $10\,dB$. Given the standard deviation of simulated measurement noise σ_y, the SNR can be defined as

$$\mathrm{SNR} \triangleq 10\log_{10}(N^{-1} \textstyle\sum_{k=1}^{N} \mathrm{SNR}_k) \qquad (35)$$

where: $\mathrm{SNR}_k \triangleq N_h^{-1} \sum_{h=1}^{N_h} \sigma_y^{-2} x_{k,h}^2$; $x_{k,h}$ is the acoustic pressure on the h-th sensor at time k; N is the total number of time integration steps. In this scenario, the source starts to emit at time $t = 0\,s$ while the data assimilation process is activated when the array starts to collect data, i.e. at time $t^0 = 0.8\,s$ when the acoustic wave has already reached the VA of hydrophones. Performance of the filter, in terms of detection and localization, is shown in Fig. 7. It can be seen how no detection is unveiled until $t^* = 1.516\,s$, when the array measurements begin to correctly match the predicted measurements $\hat{\boldsymbol{y}}_k^e$ generated from the model associated to e^s. The mode in operation before t^* is $\hat{e}_k = 0$, i.e. the no-source mode, while $\hat{e}_k = e^s, k \geq t^*$, i.e. the true mode in operation e^s is correctly detected starting from time t^*. Once the source mode is estimated, the localization process within the source element is activated. Furthermore, in Fig. 7 the distance between the estimated position $\hat{\boldsymbol{p}}_{k|k}^s$ and the true source position $\boldsymbol{p}^s$ is plotted versus time, compared to the distance obtained with the MVDF-MFP for the same dataset. It can be seen how the proposed algorithm yields better localization accuracy than the MVDF-MFP over the whole simulation time. In Fig. 8 we see that when the local EnKF is activated and the estimation is performed within the selected element e^s, the initial distance corresponding to the center of the element becomes even smaller and the source localization performance further improves. Indeed, the position samples $\hat{\boldsymbol{p}}_{k|k}^{s,i,e}$ (displayed in red) initially distributed all over the source element Ω_{e^s}, and their average $\hat{\boldsymbol{p}}_{k|k}^s$ (displayed in blue) gets closer to the true source position $\boldsymbol{p}^s$ (displayed in magenta) with a final offset of about $3\,m$. Fig. 9 provides several plots comparing the estimated and ground-truth acoustic fields over the domain Ω_d at different time instants. Such fields can be compared to the ambiguity surface $A(\boldsymbol{p}^s)$ provided by MVDF-MFP in Fig. 10 using a grid of $N_s = 13800$ possible source position hypotheses. Notice that the maximum value of $A(\cdot)$, surrounded by a red box, coincides with the estimated source position provided by MVDF-MFP.

Furthermore, for the same environmental configuration but with source frequency $f_s = 30\,Hz$, $\Delta L_g = 15\,m$ and $\Delta L_f = 30\,m$, we evaluated the performance of the FMM-SE-EnKF in terms of time-averaged root mean square error of the estimated source position (RMSE_{pos}). Position RMSE is defined as

$$\mathrm{RMSE}_{pos} \triangleq N^{-1} \textstyle\sum_{k=k^*}^{N} \mathrm{RMSE}_{pos,k} \qquad (36)$$

where k^* is the discrete time instant corresponding to t^* and $\mathrm{RMSE}_{pos,k}$ is the error at time k defined as

$$\mathrm{RMSE}_{pos,k} \triangleq \sqrt{M^{-1} \textstyle\sum_{r=1}^{M} (\hat{\boldsymbol{p}}_{k|k,r}^s - \boldsymbol{p}^s)} \qquad (37)$$
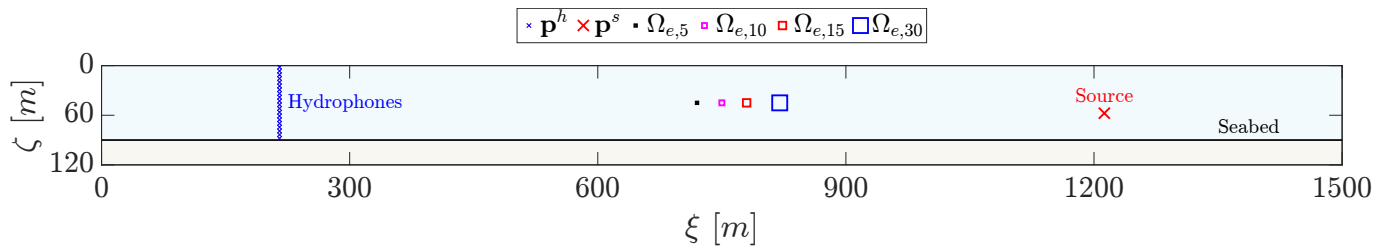
Fig. 5: Environment configuration of the waveguide with regular seabed within the domain Ω_d. Elements $\Omega_{e,l}$ with different side lengths l in meters, used for the ground-truth and filter mesh, are compared.
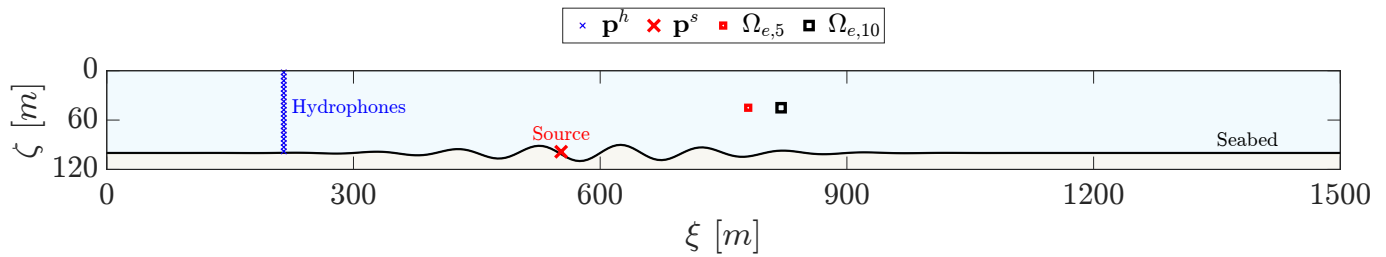

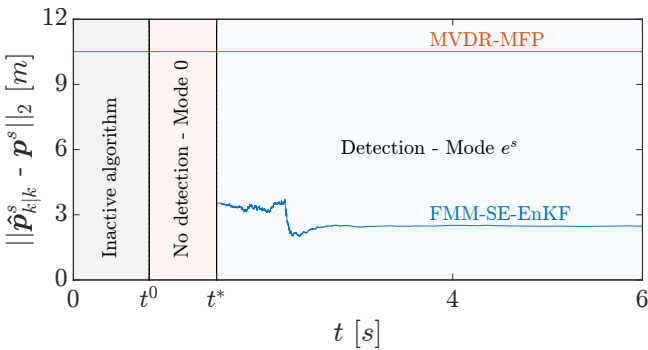Fig. 6: Environment configuration of the waveguide with irregular seabed within the domain Ω_d.

Fig. 7: Mode detection trend, and distance between estimated source position $\hat{\boldsymbol{p}}_{k|k}^s$ and true source position $\boldsymbol{p}^s$, versus distance provided by MVDR-MFP algorithm for the scenario with regular seabed.

RMSE$_{pos}$ vs. SNR				
SNR [dB]	-10	-5	0	5	10
RMSE$_{pos}$ [m]	3.6734	3.2249	2.9095	2.7693	2.7526

RMSE$_{pos}$ vs. N_h				
N_h	10	20	30	40	50
RMSE$_{pos}$ [m]	3.7406	2.7526	2.3446	2.1077	1.9664

RMSE$_{pos}$ vs. d_{hs}				
d_{hs} [m]	400	600	800	1000	1200
RMSE$_{pos}$ [m]	0.5012	0.9383	1.928	2.7526	4.9588

TABLE IV: RMSE$_{pos}$ versus SNR, N_h, d_{hs}.

$\hat{\boldsymbol{p}}_{k|k,r}^s$ being the estimated source position at time k for the r-th Monte Carlo run, and $M = 50$ the total number of Monte Carlo runs. Table IV reports the position RMSE performance for five different levels of SNR, a VA of $N_h = 20$ hydrophones located at a range distance $d_{hs} = 1000\,m$ from the source. It can be seen that source localization turns out to be satisfactory at all levels of SNR. Furthermore, Table IV also provides position RMSE for a VA with a varying number $N_h \in \{10, 20, 30, 40, 50\}$ of hydrophones, $SNR = 10$ dB and distance from the source $d_{hs} = 1000\,m$. In this case, it can be seen how performance clearly improves as the number of sensors increases. Notice that the reported simulations also show how the space between sensors affects performance. In fact, in the performed Monte Carlo simulations, the N_h sensors were regularly spaced to span the entire $90\,[m]$ depth of the surveiled water column so that, for each value of N_h, a different space among sensors of $d_{hh}^* = 90/N_h\,[m]$ is considered. We remark that the choice of varying sensor number N_h and sensor spacing d_{hh} while keeping constant the product $N_h d_{hh}$

is motivated by the considerations that: decreasing the inter-sensor distance d_{hh} for fixed N_h would reduce the depth span of the vector array with consequent deterioration of localization performance; increasing d_{hh} above d_{hh}^* would actually reduce the number of effective sensors leaving some of them out of the water column of interest. Finally, Table IV compares the position RMSE for different distances d_{hs} of the array from the source, with fixed SNR$= 10\,dB$ and number of sensors $N_h = 20$, showing how localization performance significantly improves when the sensor array gets closer to the source.

As a final remark, we point out that the model used in the filter is different from the one used to generate the data (see the different parameters of the two meshes in Table II), thus showing that the proposed approach is able to provide satisfactory performance even under model mismatch.

B. Scenario with irregular seabed

This second scenario involves a motionless source located at $\xi = 552.5\,m$, $\zeta = 98.5\,m$ (very close to the seabed) emitting a signal of frequency $f_s = 100\,Hz$ for a simulation time
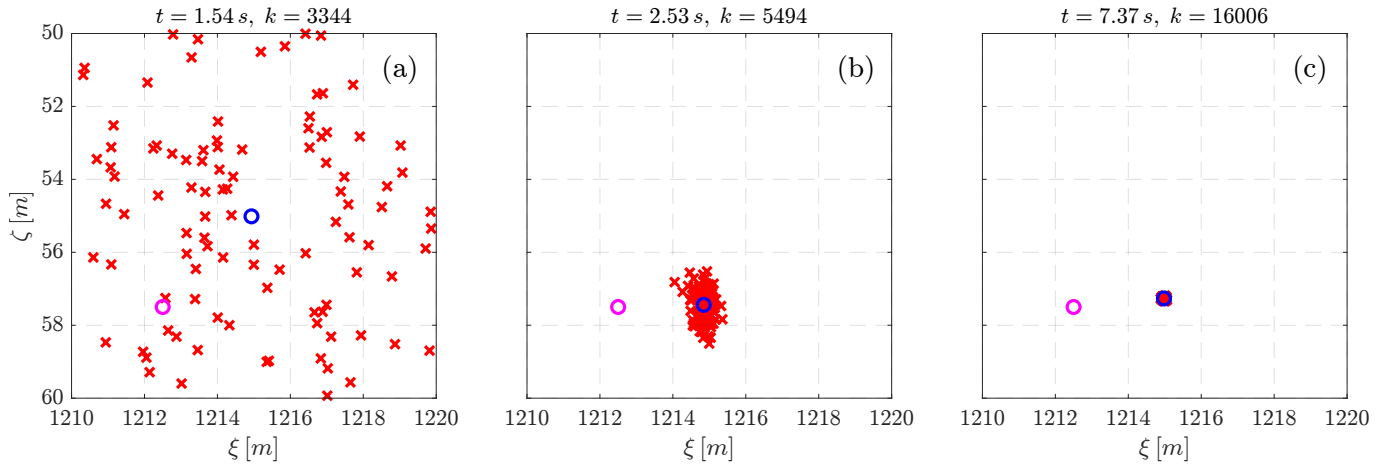
Fig. 8: (a, b, c) Position samples $\hat{\mathbf{p}}_{k|k}^{s,i,e}$ (in red), estimated position $\hat{\mathbf{p}}_{k|k}^{s,e}$ (in blue), and true source position $\mathbf{p}^s$ (in magenta) within the source element domain Ω_{e^s} at different time steps for the simulated scenario with regular seabed.
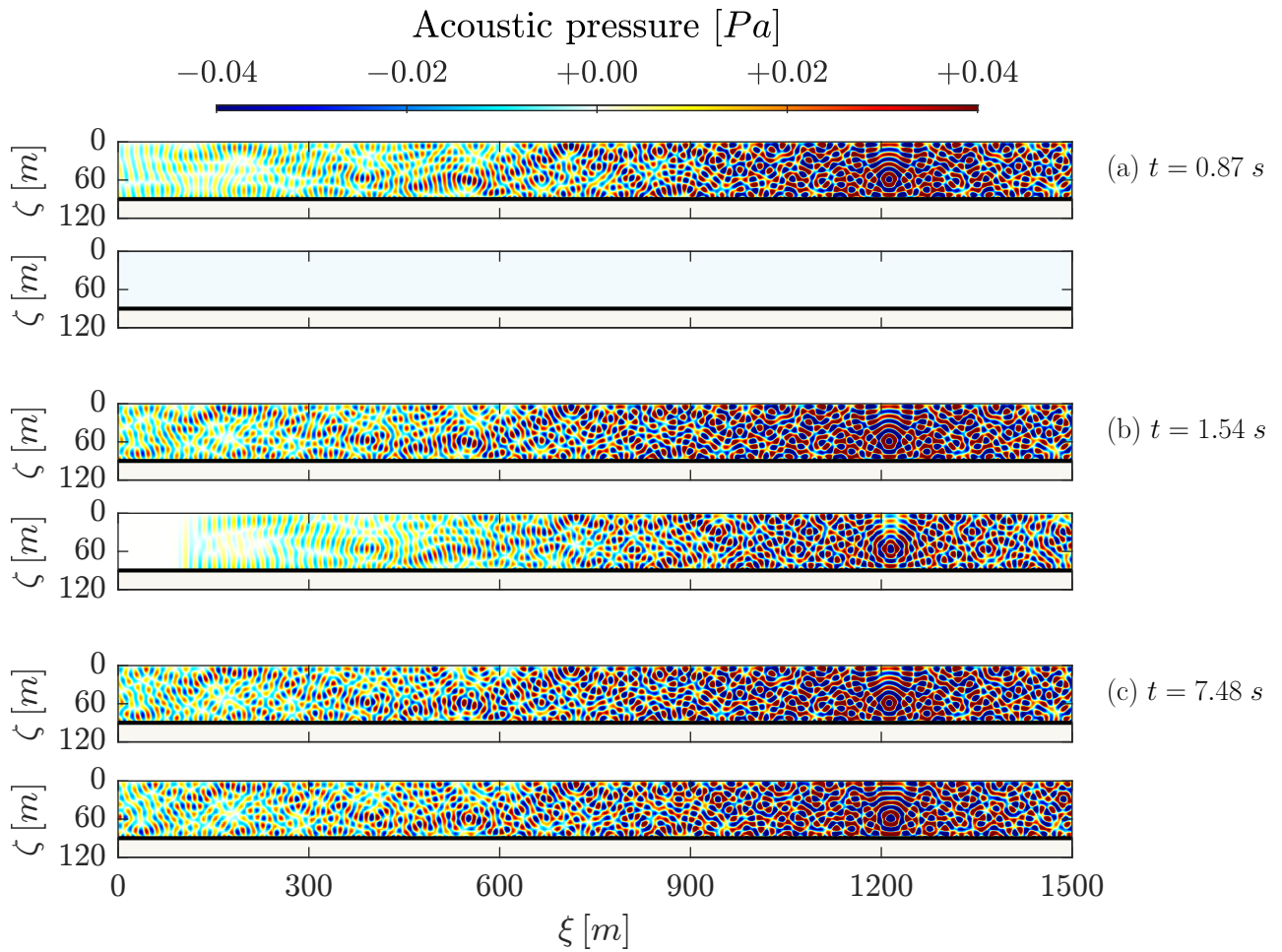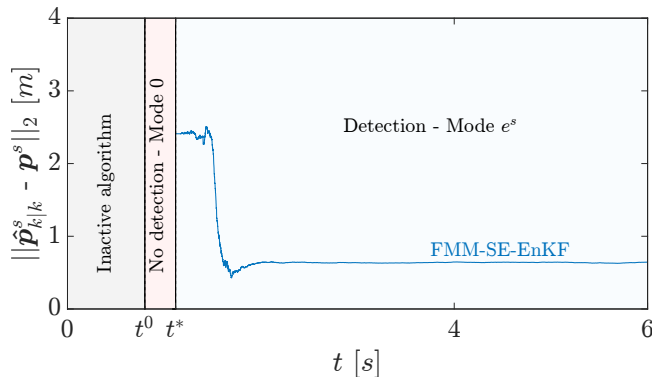

Fig. 9: Comparison of ground-truth simulator acoustic field $\boldsymbol{x}_k$ (upper plot) and estimated acoustic field $\hat{\boldsymbol{x}}_{k|k}$ (lower plot) by the Fast MM-SE-EnKF algorithm at different times, for the scenario with regular seabed.
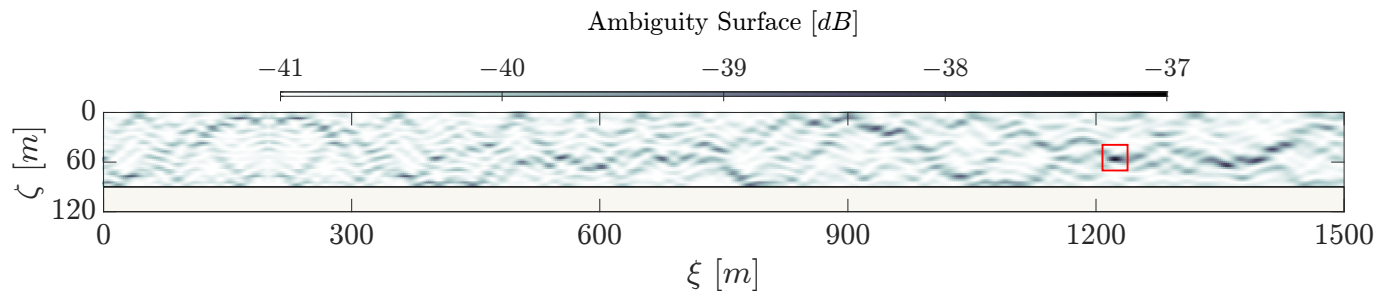
Fig. 10: Ambiguity surface $A(\boldsymbol{p}^s)$ for the scenario with regular seabed provided by the MVDF-MFP algorithm where the maximum value is surrounded by a red box.

Fig. 11: Mode detection trend, and distance between estimated source position $\hat{\boldsymbol{p}}^s_{k|k}$ and true source position $\boldsymbol{p}^s$, for the scenario with irregular seabed.

of $10\,s$ with step integration time $\Delta t = 0.23\,ms$, within a rectangular domain Ω_d with depth of $100\,m$, range of $1500\,m$, and irregular seabed. The environment scenario, depicted in Fig. 6, presents an isospeed configuration ($\rho = 1000$ Kg/m^3, $c = 1500$ m/s, $\alpha = 4 \times 10^{-6}$ s/m^2). Table II provides the parameters of the mesh for the ground-truth simulator and the filter. Parameters used for the FMM-SE-EnKF algorithm are reported in Table III. Also in this case, as for the previous scenario, we chose the size of the square mesh element of the filter such that MSR$= 0.5$. In Fig. 11 the performance of the filter, in terms of both source detection and localization, is illustrated. It can be seen how data assimilation starts at $t^0 = 0.8\,s$, and at time $t^* = 1.119\,s$, the filter is able to detect the signal and localization is satisfactorily performed as the mode in operation $\hat{e}_k$ matches the source element e^s after the detection of the source signal. Once the source element Ω_e has been detected, the filter runs a local EnKF for finer localization within Ω_{e^s}. Furthermore, Fig. 11 plots, versus time, the distance between true, $\boldsymbol{p}^s$, and estimated, $\hat{\boldsymbol{p}}^s_{k|k}$, source locations. It can be observed how the local run of the EnKF enhances localization accuracy starting from an initial position coinciding with the element center. This behaviour is verified in Fig. 12, where we can see the position samples $\hat{\boldsymbol{p}}^{s,i,e}_{k|k}$ for the source mode e^s moving, within the element $\Omega_{\hat{e}} = \Omega_{e^s}$ during the data assimilation process, towards the true source position $\boldsymbol{p}^s$. Finally, Fig. 13 provides some snapshots of the estimated field $\hat{\boldsymbol{x}}_{k|k}$ compared to the simulated field $\boldsymbol{x}_k$ at different time instants.

VI. CONCLUSION

In this work, we proposed a *fast multiple model spectral element ensemble Kalman filter* (FMM-SE-EnKF), a new *multiple model* (MM) algorithm specifically devised for acoustic *underwater source localization* (USL) in shallow water. Such algorithm combines a *spectral element method* (SEM)-based propagation model and Bayesian field estimation for large-scale systems. Unlike approaches based on *matched field processing* (MFP), the proposed FMM-SE-EnKF can cope with more general space-time varying underwater environments. In this work, it has been demonstrated how this algorithm can effectively perform detection and localization in the case of irregular seabed. Future work will concern extensions to: (1) moving sources; (2) space-time varying speed of sound and/or density; (3) three-dimensional environments.

REFERENCES

[1] F.B. Jensen, W.A. Kuperman, M.B. Porter, and H. Schmidt, *Computational ocean acoustics*. Springer New York, New York, NY, 2011.

[2] D. Abraham, *Underwater acoustic signal processing: modeling, detection, and estimation*. Springer, 2019.

[3] H. Krim, and M. Viberg, "Two decades of array signal processing research: the parametric approach," *IEEE Signal Processing Magazine*, vol. 13, no. 4, pp. 67-94, 1996.

[4] H. S. Lim, B. P. Ng, and V. V. Reddy, "Generalized MUSIC-like array processing for underwater environments," *IEEE Journal of Oceanic Engineering*, vol. 42, no. 1, pp. 124-134, 2017.

[5] A. Gunes, and M. B. Guldogan, "Joint underwater target detection and tracking with the Bernoulli filter using an acoustic vector sensor," *Digital Signal Processing*, vol. 48, pp. 246-258, 2016.

[6] K. Naganananda, and G. Anand, "Underwater target tracking with vector sensor array using acoustic field measurements," in *Proc. OCEANS*, 2017.

[7] W. Yi, L. Fu, A. F. Garcia-Fernandez, L. Xu, and L. Kong, "Particle filtering based track-before-detect method for passive array sonar systems," *Signal Processing*, vol. 165, pp. 303-314, 2019.

[8] R. J. Vaccaro, "The past, present, and the future of underwater acoustic signal processing," *IEEE Signal Processing Magazine*, vol. 15, pp. 21-51, 1998.

[9] A. B. Baggeroer, W. A. Kuperman, and H. Schmidt, "Matched field processing: source localization in correlated noise as an optimum parameter estimation problem," *The Journal of the Acoustical Society of America*, vol. 83, no. 2, pp. 571-587, 1988.

[10] A. B. Baggeroer, W. A. Kuperman, and P. N. Mikhalevsky, "An overview of matched field methods in ocean acoustics," *IEEE Journal of Oceanic Engineering*, vol. 18, no. 4, pp. 401-424, 1993.

[11] A. Tolstoy, *Matched field processing for underwater acoustics*. World Scientific, 1993.

[12] G. Zhu, Y. Wang, and Q. Wang, "Matched field processing based on Bayesian estimation," *Sensors*, vol. 20, no. 5, 2020.

[13] A. Tolstoy, "Sensitivity of matched field processing to sound-speed profile mismatch for vertical arrays in a deep Pacific environment," *J. Acoust. Soc. Am.*, vol. 85, no. 6, pp. 2394-2404, 1989.
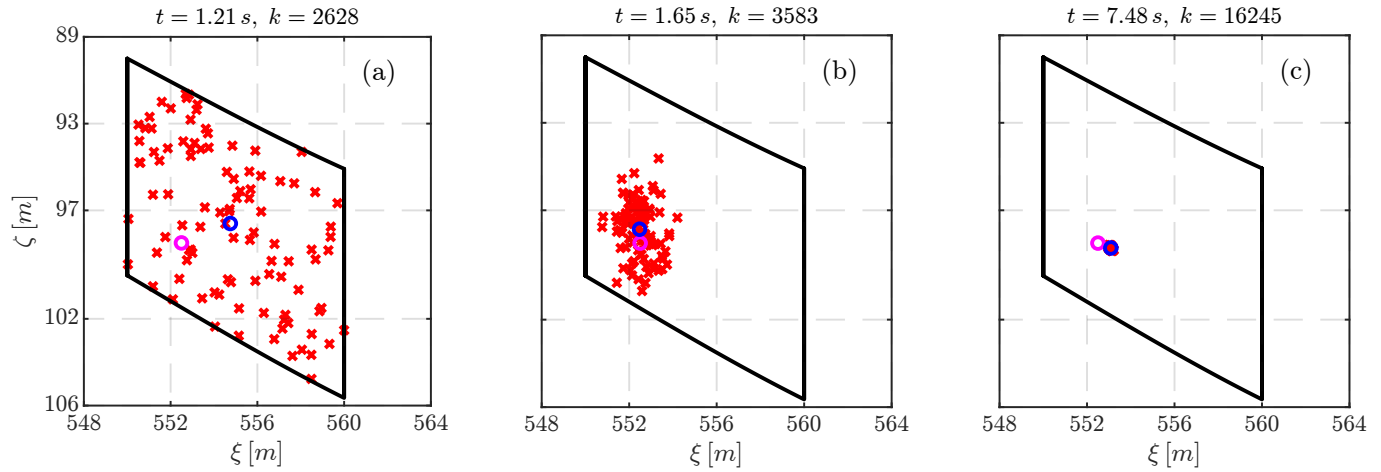
Fig. 12: (a, b, c) Position samples $\hat{\mathbf{p}}_{k|k}^{s,i,e}$ (in red), estimated position $\hat{\mathbf{p}}_{k|k}^{s,e}$ (in blue), and true source position $\mathbf{p}^s$ (in magenta) within the source element domain Ω_{e^s} at different time steps for the simulated scenario with irregular seabed.
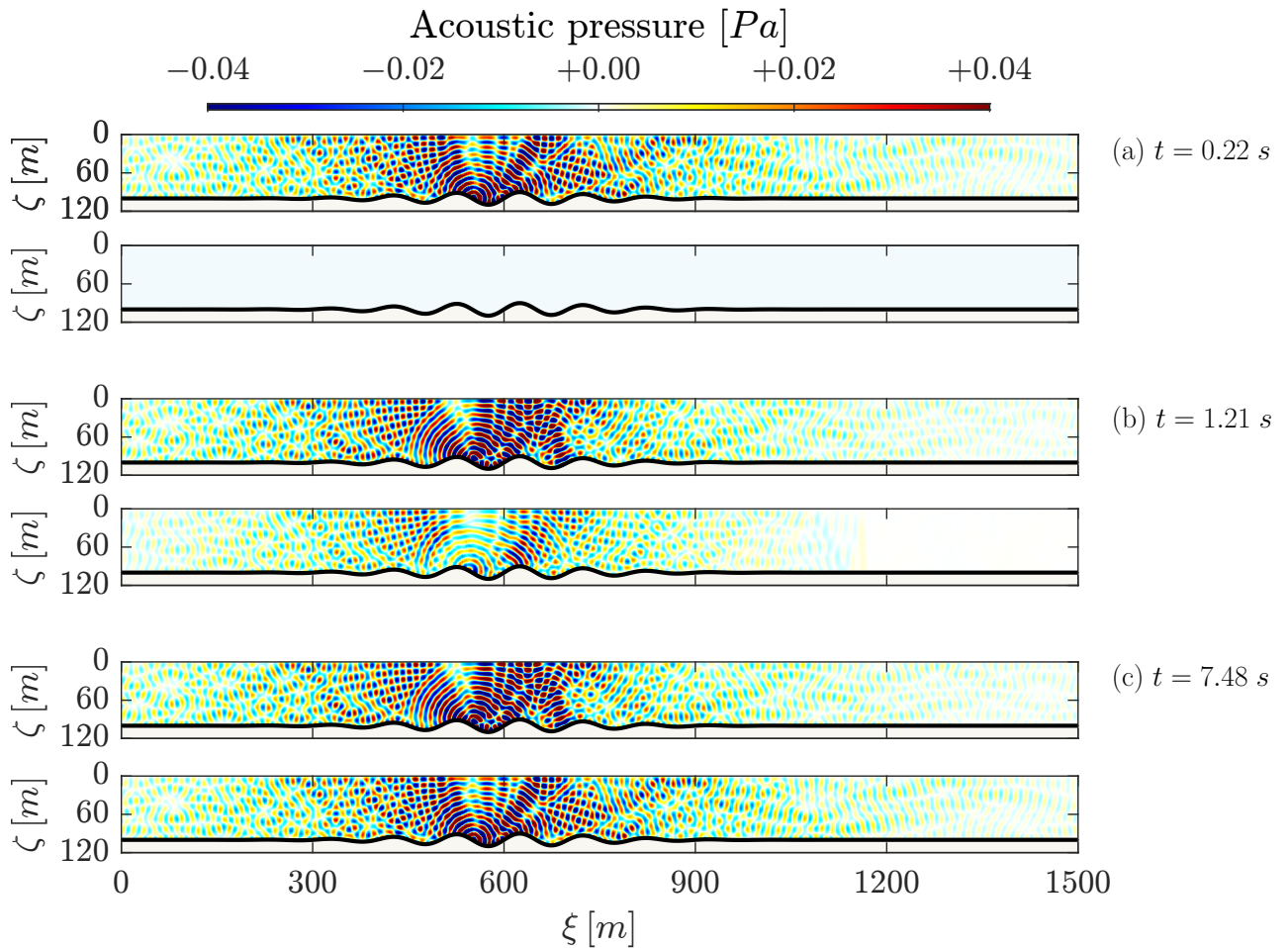

Fig. 13: Comparison of ground-truth simulator acoustic field $\boldsymbol{x}_k$ (upper plot) and estimated acoustic field $\hat{\boldsymbol{x}}_{k|k}$ (lower plot) by the Fast MM-SE-EnKF algorithm at different times, for the scenario with irregular seabed.

[14] E. C. Shang, and Y. Y. Wang, "Environmental mismatching effects on source localization processing in mode space," *The Journal of the Acoustical Society of America*, vol. 89, no. 5, pp. 2285-2290, 1991.

[15] S. L. Tantum, and L. W. Nolte, "Tracking and localizing a moving source in an uncertain shallow water environment," *The Journal of the Acoustical Society of America*, vol. 103, no. 1, pp. 362-373, 1998.

[16] D. Tollefsen, and S. E. Dosso, "Source localization with multiple hydrophone arrays via matched-field processing," *IEEE Journal of Oceanic Engineering*, vol. 42, no. 3, pp. 654-662, 2017.

[17] D. Tollefsen, P. Gestorft and W. S. Hodgkiss, "Multiple-array passive acoustic source localization in shallow water," *The Journal of the Acoustical Society of America*, vol. 141, no. 3, pp. 1501-1513, 2017.

[18] D. Komatitsch, and J. Tromp, "Introduction to the spectral element method for three-dimensional seismic wave propagation," *Geophysical Journal International*, vol. 139, no. 3, pp. 806-822, 12 1999.

[19] D. Komatitsch, C. Barnes, and J. Tromp, "Wave propagation near a fluid-solid interface: a spectral-element approach," *GEOPHYSICS*, vol. 65, no. 2, pp. 623-631, 2000.

[20] P. Cristini, and D. Komatitsch, "Some illustrative examples of the use of a spectral-element method in ocean acosutics," *The Journal of the Acoustical Society of America*, vol. 131, no. 3, pp. EL229-EL235, 2012.

[21] D. Komatitsch, and J. P. Vilotte, "The spectral element method: an efficient tool to simulate the seismic response of 2D and 3D geological structures," *Bulletin of the Seismological Society of America*, vol. 88, no. 2, pp. 368-392, 04 1998.

[22] R. Sabatini, O. Marsden, C. Bailly, and O. Gainville, "Three-dimensional direct numerical simulation of infrasound propagation in the Earth's atmosphere," *Journal of fluid mechanics*, vol. 859, pp. 754-789, 2019.

[23] G. Battistelli, L. Chisci, N. Forti, G. Pelosi, and S. Selleri, "Distributed finite-element Kalman filter for field estimation," *IEEE Transactions on Automatic Control*, vol. 62, no. 7, pp. 3309-3322, 2017.

[24] Z. Li, K. You, and S. Song, "Cooperative field prediction and smoothing via covariance intersection," *IEEE Transactions on Signal Processing*, vol. 69, pp. 797-808, 2021.

[25] G. Battistelli, L. Chisci, N. Forti, G. Pelosi, and S. Selleri, "Point source estimation via finite element multiple-model Kalman filtering," in *Proc. 54th IEEE Conference on Decision and Control*, pp. 4984-4989, 2015.

[26] N. Forti, L. Gao, G. Battistelli, and L. Chisci, "Unknown source in spatially distributed systems: identifiability analysis and estimation," *Automatica*, vol. 136, pp. 110025, 2022.

[27] A. Weiss, T. Arikan, H. Vishnu, G. B. Deane, A. C. Singer, and G. W. Wornell "A semi-blind method for localization of underwater acoustic sources," *IEEE Transactions on Signal Processing*, vol. 70, pp. 3090-3106, 2022.

[28] P. S. Rossi, D. Ciuonzo, T. Ekman and H. Dong, "Energy detection for MIMO decision fusion in underwater sensor networks," *IEEE Sensors Journal*, vol. 15, no. 3, pp. 1630-1640, 2015.

[29] L. Hu, X. Wang, and S. Wang, "Decentralized underwater target detection and localization," *IEEE Sensors Journal*, vol. 21, no. 2, pp. 2385-2399, 2021.

[30] X. Zhu, H. Dong, P. S. Rossi, and M. Landrø, "Matched field processing based on Bayesian estimation," *IEEE Sensors Journal*, vol. 22, no. 13, pp. 13299-13308, 2022.

[31] C. Drioli, G. Giordano, D. Salvati, F. Blanchini, and G.L. Foresti, "Acoustic target tracking through a cluster of mobile agents," *IEEE Transactions on Cybernetics*, vol. 51, no. 5, pp. 2587-2600, 2021.

[32] G. Evensen, *Data assimilation: the ensemble Kalman filter*. Springer Science & Business Media, 2009.

[33] G.A. Manduzio, N. Forti, R. Sabatini, P. Braca, G. Battistelli, and L. Chisci, "Dynamic source localization via finite-element underwater acoustic field estimation," in *Proc. 29th European Signal Processing Conference (EUSIPCO)*, pp. 226–230, 2021.

[34] A. Fichtner, *Full seismic waveform modelling and inversion*. Springer Berlin, Heidelberg, 2011.

[35] Y. Bar-Shalom, X.R. Li, and T. Kirubarajan, *Estimation with applications to tracking and navigation*. John Wiley & Sons, 2001.

[36] G. Evensen, "The ensemble Kalman filter: theoretical formulation and practical implementation," *Ocean dynamics*, vol. 53, no. 4, pp. 343–367, 2003.

[37] R. Sabatini and P. Cristini, "A multi-domain collocation method for the accurate computation of normal modes in open oceanic and atmospheric waveguides," *Acta Acustica united with Acustica*, vol. 105, no. 3, pp. 464–474, 2019.

[38] M. Roth, G. Hendeby, C. Fritsche and F. Gustafsson, "The ensemble Kalman filter: a signal processing perspective," *Eurasip Journal on Advances in Signal Processing*, no. 56, 2017, DOI 10.1186/s13634-017-0492-x.

[39] M.B. Porter and A. Tolstoy, "The matched field processing benchmark problems," *Journal of Computational Acoustics*, vol. 2, no. 3, pp. 161–185, 1994.

Graziano A. Manduzio received the B.Sc. degree in electronic and telecommunication engineering, and the M.Sc. degree in automation engineering from the University of Florence, Florence, Italy, in 2013 and 2018, respectively. In 2023, he received the Ph.D. degree in information engineering from the University of Pisa, Pisa, Italy. In 2020, he was a Visiting Researcher with the NATO Centre for Maritime Research and Experimentation (CMRE), La Spezia, Italy. He is currently a Postdoctoral Researcher in the Department of Information Engineering at the University of Pisa. His main research interests include Bayesian estimation, machine learning and robotics.

Nicola Forti received the M.S. degree in automation engineering and the Ph.D. degree in information engineering from the University of Florence, Florence, Italy, in 2013 and 2016, respectively. In 2015-16, he was a Visiting Researcher in the Department of Electrical and Computer Engineering at Carnegie Mellon University, Pittsburgh, PA, USA. From 2018 to 2023, he held the position of Scientist with the NATO Centre for Maritime Research and Experimentation (CMRE), La Spezia, Italy. He is currently an Assistant Professor in the Department of Information Engineering at the University of Florence, Florence, Italy. His main research interests include state estimation, networked control systems, data fusion, and learning systems. Dr. Forti also serves as an Editor for the International Journal of Adaptive Control and Signal Processing.

Roberto Sabatini was born in Avezzano, Italy, in 1987. In 2013, he received an M.S. degree in aerospace engineering from the Politecnico di Torino, Torino, Italy, and an M.S. degree in general engineering from the École Centrale de Lyon, Écully (Lyon), France. In 2017, he received a Ph.D. degree in Fluid Mechanics and Acoustics from the École Centrale de Lyon. Since 2021, Dr. Sabatini has been an Assistant Professor of Engineering Physics with the Department of Physical Sciences at Embry-Riddle Aeronautical University, Daytona Beach, Florida, USA. Dr. Sabatini has over a decade of experience in the theory and modeling of the nonlinear propagation of mechanical waves in complex environments, such as the atmosphere or the ocean, as well as in the design of numerical methods suitable for the resolution of the equations governing such waves. He developed parallelized codes for clusters of CPUs and GPUs (in C, C++, OpenCL, CUDA, MPI) for the numerical resolution of different systems of partial differential equations, like the compressible unsteady Navier-Stokes equations, the equations of continuum mechanics, the wave equation, the parabolic approximation of the wave equation, and the equations describing the evolution of instabilities in compressible flows.

Giorgio Battistelli received the Laurea degree in electronic engineering and the Ph.D. degree in robotics from the University of Genoa, Genoa, Italy, in 2000 and 2004, respectively. From 2004 to 2006, he was a Research Associate with the Dipartimento di Informatica, Sistemistica e Telematica, University of Genoa.

Since 2006 he has been with the University of Florence, Florence, Italy, where he is currently a Full Professor of automatic control and vice head of the Department of Information Engineering. His current research interests include adaptive and learning systems, linear and nonlinear estimation, sensor networks, and information fusion.

Dr. Battistelli was a member of the editorial boards of the IFAC journals Engineering Applications of Artificial Intelligence and Nonlinear Analysis: Hybrid Systems and of the IEEE Transactions on Neural Networks and Learning Systems. He is currently an Associate Editor of the IEEE Control Systems Letters.

Luigi Chisci was born in Florence, Italy, in 1959. He received the M.S. degree in electrical engineering from the University of Florence, Florence, Italy, in 1984 and the Ph.D. degree in systems engineering from the University of Bologna, Bologna, Italy, in 1989. Since December 2004, he is Full Professor of control engineering with the University of Florence. His educational and research career have been in the area of control and systems engineering. His research interests have spanned over adaptive control and signal processing, algorithms and architectures for real-time control and signal processing, recursive identification, filtering and estimation, and predictive control. His current interests concern networked estimation, multi-target multi-sensor tracking, multi-agent systems, and sensor data fusion. He has co-authored more 100 papers published on international journals. Dr. Chisci was on the Conference Editorial Board of the IEEE Control Systems Society as an Associate Editor, from 2000 to 2008. He is currently Associate Editor of the IEEE Transactions on Aerospace and Electronic Systems and in the Editorial Board of the International Journal of Adaptive Control and Signal Processing.